MIT Open Access Articles

Viriato : A Fourier–Hermite spectral code for strongly magnetized fluid–kinetic plasma dynamics

Massachusetts Institute of Technology

`Viriato`: a Fourier-Hermite spectral code for strongly magnetised fluid-kinetic plasma dynamics

N. F. Loureiro[a,*], W. Dorland[b], L. Fazendeiro[a], A. Kanekar[b], A. Mallet[c],
M. S. Vilelas[a], A. Zocco[d]

[a]*Instituto de Plasmas e Fusão Nuclear, Instituto Superior Técnico, Universidade de Lisboa, 1049-001 Lisboa, Portugal*
[b]*IREAP & Department of Physics, University of Maryland, College Park, MD 20742, USA*
[c]*Rudolf Peierls Centre for Theoretical Physics, University of Oxford, Oxford OX1 3NP, United Kingdom*
[d]*Max-Planck-Institut für Plasmaphysik, Wendelsteinstrasse, D-17489, Greifswald, Germany*

Abstract

We report on the algorithms and numerical methods used in `Viriato`, a novel fluid-kinetic code that solves two distinct sets of equations: (i) the Kinetic Reduced Electron Heating Model (KREHM) equations [Zocco & Schekochihin, Phys. Plasmas **18**, 102309 (2011)] (which reduce to the standard Reduced-MHD equations in the appropriate limit) and (ii) the kinetic reduced MHD (KRMHD) equations [Schekochihin *et al.*, Astrophys. J. Suppl. **182**:310 (2009)]. Two main applications of these equations are magnetised (Alfvénic) plasma turbulence and magnetic reconnection. `Viriato` uses operator splitting (Strang or Godunov) to separate the dynamics parallel and perpendicular to the ambient magnetic field (assumed strong). Along the magnetic field, `Viriato` allows for either a second-order accurate MacCormack method or, for higher accuracy, a spectral-like scheme composed of the combination of a total variation diminishing (TVD) third order Runge-Kutta method for the time derivative with a 7th order upwind scheme for the fluxes. Perpendicular to the field `Viriato` is pseudo-spectral, and the time integration is performed by means of an iterative predictor-corrector scheme. In addition, a distinctive feature of `Viriato` is its spectral representation of the parallel velocity-space dependence, achieved by means of a Hermite representation of the perturbed distribution function. A series of linear and nonlinear benchmarks and tests are presented, including a detailed analysis of 2D and 3D Orszag-Tang-type decaying turbulence, both in fluid and kinetic regimes.

Keywords:
PACS: 52.30.Gz, 52.65.Tt, 52.35.Vd, 52.35.Ra

*Corresponding author
    Email address: nloureiro@ipfn.ist.utl.pt (N. F. Loureiro)
    URL: http://web.ist.utl.pt/nuno.f.loureiro (N. F. Loureiro)

1. Introduction

Magnetised plasma dynamics lies at the heart of many fascinating phenomena in astro, space and laboratory physics. Turbulence in the solar wind [1] and in the interstellar medium [2], solar [3], stellar [4] and accretion disk flares [5], substorms in the Earth's magnetosphere [6], and turbulent transport and instabilities in magnetised fusion experiments [7], are just a few examples of remarkable physics problems whose solution is indeed determined by understanding the behaviour of plasmas in a magnetised environment.

In many of these cases, (i) the collision frequency is much lower than the typical frequencies of the physical phenomena of interest (e.g., turbulence, magnetic reconnection) — i.e., the plasmas are weakly collisional; and (ii) the size of the ion Larmor orbit is several orders of magnitude smaller than the size of the system. Weak collisionality implies that on the timescales of interest the plasma cannot be treated as a fluid, and instead a kinetic description that evolves the particles' distribution functions is required. This is rather unfortunate from the computational point of view, since fully kinetic models live on a six-dimensional phase-space (each particle is characterised by its position and velocity vectors). The strong magnetisation, however, implies that the plasma is highly anisotropic, with very different particle motions along and across the magnetic field direction. This anisotropy can be explored analytically to yield reduced kinetic models, i.e., asymptotic descriptions that reduce the phase-space to only 5D or even 4D. This leads to tremendous computational savings and effectively renders possible calculations that would otherwise not be feasible on today's supercomputers.

Gyrokinetics [8, 9, 10, 11, 12] is a rigorous description of strongly magnetised, weakly-collisional plasmas. The key idea behind the gyrokinetic formalism is that, because of the strong magnetic (guide) field, the particles' Larmor gyration frequency is much higher than the frequencies of dynamical interest, and can thus be averaged over. This allows for the reduction of the dimensionality of the system, from 6D (three position and three velocity coordinates) to 5D (three position coordinates, and velocities parallel and perpendicular to the magnetic field) while retaining all the essential physical effects. Gyrokinetics was originally motivated by the attempt to model microinstabilities in magnetic fusion experiments; in this respect it has been rather successful [10, 11]. As recognition of its usefulness, the range of applications of gyrokinetics has broadened in recent years; it is now routinely applied to the study of turbulence in magnetised astrophysical systems [9, 13, 14, 15], and there have also been some studies pioneering its application to the problem of magnetic reconnection [16, 17, 18, 19, 20].

This reduction of the dimensionality of the system allowed by gyrokinetics is extremely advantageous from the numerical point of view. Nonetheless, intrinsically multiscale problems such as kinetic turbulence and reconnection remain formidable computational challenges. Further simplification where possible is therefore desirable.

One possible such simplification of gyrokinetics has recently been proposed

by Zocco and Schekochihin [21]: the Kinetic Reduced Electron Heating Model (KREHM), a rigorous asymptotic limit of gyrokinetics valid for plasmas such that

$$\beta_e \sim m_e/m_i, \tag{1}$$

where $\beta_e = 8\pi n_{0e}T_{0e}/B_0^2$ is the electron beta, n_{0e}, T_{0e} are the background electron density and temperature, respectively, and B_0 is the background magnetic field. Under this assumption, Ref. [21] shows that it is possible to reduce the plasma dynamics to a 4D phase-space — position and velocity parallel to the magnetic field — while retaining key physics such as phase-mixing and electron Landau damping, ion finite Larmor radius effects, electron inertia, electron collisions and Ohmic resistivity. This is a very significant simplification of the full kinetic description, which renders possible truly multiscale kinetic simulations. In particular, because no *ad hoc* fluid closure is employed, KREHM can be used for detailed studies of energy conversion and dissipation in kinetic turbulence and reconnection, including electron heating via phase-mixing and Landau damping.

If taken literally, the ordering imposed by equation (1) is somewhat restrictive, and obviously excludes many plasmas of interest. Examples of plasmas where it may hold are some regions of the solar corona [22, 23], the LArge Plasma Device (LAPD) experiment at UCLA [24], and edge regions in some tokamaks [25][1]. However, one may legitimately expect that the plasma behaviour captured by KREHM will qualitatively hold beyond its rigorous limits of applicability, as is so often the case with many other simplified plasma models (MHD being a notorious example of a description known to work rather well far outside its strict limits of validity). Hints that this may indeed be the case are offered in section 7.3, where a direct comparison of KREHM with a (non-reduced) gyrokinetic model for the linear collisionless tearing mode problem yields very good agreement at values of β_e significantly larger than m_e/m_i.

This paper reports on the numerical methods and algorithms used in `Viriato`, the first numerical code to solve this particular set of equations. An extensive series of tests and benchmarks is also presented. Considerable attention is devoted to Orszag-Tang-type decaying turbulence, both in the fluid and kinetic regimes. The reader interested in the application of this code and physics model to the problem of magnetic reconnection is referred to [26], where the importance of electron heating via Landau damping in reconnection is demonstrated for the first time.

A second set of equations solved by `Viriato` are the kinetic reduced MHD (KRMHD) equations [14], which describe the evolution of compressible fluctuations (density and parallel magnetic field) in the regime $k_\perp \rho_i \ll 1$ ($k_\perp$ being the wave number perpendicular to the guide-field of a typical perturbation, and ρ_i the ion Larmor radius.) These equations are structurally identical to those

---

[1] We hasten to add that it is unclear whether the fundamental approximations of standard gyrokinetics are at all valid in the edge region of tokamaks; however, if they are, then KREHM may be a good approximation there given that β_e does tend to be rather low in this region.

of KREHM, so their numerical implementation in `Viriato` is straightforward. We also note that KREHM reduces to the standard Reduced-MHD (RMHD) set of equations [27, 28] in the appropriate limit (i.e., when the wave length of the fluctuations is much larger than all the kinetic scales). Thus, `Viriato` can also be used as a RMHD code (in either 2D or 3D slab geometry). Finally, we remark that under an isothermal closure for the electrons, KREHM reduces to the simple two-field gyrofluid model treated in Refs. [29, 30] (which is a limit of the more complete models of Snyder *et al.* [31] and of Schep *et al.* [32]).

This paper is organized as follows. Section 2 presents the different sets of equations integrated by `Viriato`. The kinetic equations are solved by means of a Hermite expansion, which requires some form of closure (or truncation). This is discussed in section 3, where an asymptotically exact nonlinear closure for the Hermite-moment hierarchy is derived. Section 4 presents the energy evolution equation for the closed KREHM model; and the normalizations that we adopt are laid out in section 5. Section 6 deals with the numerical discretization of the equations, including in section 6.2 a discussion of the implementation of a spectral-like scheme for the advection in the direction along the guide-field: a combination of an optimal third order total variation diminishing (TVD) Runge Kutta [33] for the time derivative with a seventh-order upwind scheme for the fluxes [34]. A series of linear and nonlinear benchmarks of the code are presented in section 7, with emphasis on Orszag-Tang-type decaying turbulence test cases. Finally, the main points and results of this paper are summarised in section 9. Also included for reference in Appendix A is the recently proposed modification of the KREHM model to allow for background electron temperature gradients [35].

2. Sets of Equations solved by `Viriato`

`Viriato` solves two distinct sets of equations: (i) the Kinetic Reduced Electron Heating Model (KREHM) equations [21] and (ii) the Kinetic Reduced MHD (KRMHD) equations [14]. These models are briefly discussed below; we refer the interested reader to the original references for a detailed derivation of the equations of each model.

2.1. The Kinetic Reduced Electron Heating Model (KREHM)

The Kinetic Reduced Electron Heating Model (KREHM) derived in Ref. [21] is a rigorous asymptotic reduction of standard gyrokinetics [8, 9, 10, 11, 12] applicable to plasmas that verify equation (1). In the slab geometry that we adopt, the background magnetic field (the guide-field) is assumed to be straight and uniform, $\boldsymbol{B}_0 = B_0 \boldsymbol{e}_z$. The perturbed electron distribution function, to lowest order in $\sqrt{m_e/m_i} \sim \sqrt{\beta}_e$, and in the gyrokinetic expansion, is defined as

$$\delta f_e = g_e + (\delta n_e/n_{0e} + 2v_\parallel u_{\parallel e}/v_{\mathrm{th}e}^2)F_{0e}, \tag{2}$$

where F_{0e} is the equilibrium Maxwellian, $v_{\mathrm{th}e} = \sqrt{2T_{0e}/m_e}$ is the electron thermal speed, $v_\parallel$ is the velocity coordinate parallel to the guide-field direction,

δn_e is the electron density perturbation (the zeroth moment of δf_e), and

$$u_{\|e} = -j_\| / n_{0e} e = (e/cm_e) d_e^2 \nabla_\perp^2 A_\| \tag{3}$$

is the parallel electron flow (the first moment of δf_e). In this expression, $j_\|$ is the parallel current and $A_\|$ is the parallel component of the vector potential (note that, in this model, the parallel ion flow is zero to the order that is kept in the expansion); and $d_e = c/\omega_{pe}$ is the electron skin depth, where $\omega_{pe} = \sqrt{4\pi n_{0e} e^2/m_e}$ is the electron plasma frequency. All moments of δf_e higher than δn_e and $u_{\|e}$ are contained in the "reduced" electron distribution function g_e, e.g., parallel temperature fluctuations are given by

$$\frac{\delta T_{\|e}}{T_{0e}} = \frac{1}{n_{0e}} \int d^3 \boldsymbol{v} \, \frac{2v_\|^2}{v_{\text{the}}^2} \, g_e. \tag{4}$$

For notational simplicity, let us introduce the following usual definitions:

$$\frac{d}{dt} = \frac{\partial}{\partial t} + \frac{c}{B_0} [\varphi, \ldots], \tag{5}$$

$$\hat{\boldsymbol{b}} \cdot \nabla = \frac{\partial}{\partial z} - \frac{1}{B_0} [A_\|, \ldots], \tag{6}$$

where φ is the electrostatic potential and $[\ldots, \ldots]$ denotes the Poisson bracket. The KREHM equations are [21]:

$$\frac{1}{n_{0e}} \frac{d\delta n_e}{dt} = -\hat{\boldsymbol{b}} \cdot \nabla \frac{e}{cm_e} d_e^2 \nabla_\perp^2 A_\|, \tag{7}$$

$$\frac{d}{dt} \left(A_\| - d_e^2 \nabla_\perp^2 A_\| \right) = \eta \nabla_\perp^2 A_\| - c\frac{\partial \varphi}{\partial z} + \frac{cT_{0e}}{e} \hat{\boldsymbol{b}} \cdot \nabla \left(\frac{\delta n_e}{n_{0e}} + \frac{\delta T_{\|e}}{T_{0e}} \right), \tag{8}$$

$$\frac{dg_e}{dt} + v_\| \hat{\boldsymbol{b}} \cdot \nabla \left(g_e - \frac{\delta T_{\|e}}{T_{0e}} F_{0e} \right) = C[g_e] + \left(1 - \frac{2v_\|^2}{v_{\text{the}}^2} \right) F_{0e} \hat{\boldsymbol{b}} \cdot \nabla \frac{e}{cm_e} d_e^2 \nabla_\perp^2 A_\|. \tag{9}$$

Here, η is the Ohmic diffusivity and $C[g_e]$ is the collision operator.

The perturbed electron density and the electrostatic potential are related via the gyrokinetic Poisson law [36]:

$$\frac{\delta n_e}{n_{0e}} = \frac{Z}{\tau} \left(\hat{\Gamma}_0 - 1 \right) \frac{e\varphi}{T_{0e}}, \tag{10}$$

where $\tau = T_{0i}/T_{0e}$ and $\hat{\Gamma}_0$ denotes the inverse Fourier transform of $\Gamma_0(\alpha) = I_0(\alpha)e^{-\alpha}$, with I_0 the modified Bessel function and $\alpha = k_\perp^2 \rho_i^2/2$ ($\rho_i = v_{\text{th}i}/\Omega_i$ is the ion Larmor radius, with $v_{\text{th}i} = \sqrt{2T_{0i}/m_i}$ the ion thermal velocity and $\Omega_i = ZeB_0/m_i c$ the ion gyrofrequency).

Equation (9) is a kinetic equation for the reduced electron distribution function $g_e(x, y, z, v_\parallel, v_\perp, t)$. An important observation is that it does not contain an explicit dependence on $v_\perp$. If such a dependence is not introduced by the collision operator $C[g_e]$, then $v_\perp$ can be integrated out, and the reduced electron distribution function becomes effectively 4D only, $g_e = g_e(x, y, z, v_\parallel)$.

2.1.1. Hermite expansion

The use of a Hermite polynomial expansion of the distribution function is a well-known technique to simplify the numerical solution of kinetic equations such as (9) [37, 38, 39, 40, 41, 42, 43] — see [41] in particular for an insightful discussion of this approach. A very convenient aspect of the Hermite formulation is that it enables a spectral representation of velocity space, a highly-desirable property when the available resolution is limited (as is almost invariably the case). It is worth pointing out, furthermore, that the advantages of the Hermite representation transcend the numerical aspects, as it often enables one to make analytical headway in problems that are otherwise too complex: see, e.g., Refs. [21, 44, 35, 45].

Perhaps for both these reasons, Hermite formulations have gathered considerable interest recently; we refer the reader to Ref. [46] for a very comprehensive overview of recent and past work on the subject.

The Hermite expansion of g_e is defined by

$$g_e(x, y, z, v_\parallel, t) = \sum_{m=2}^{\infty} \frac{1}{\sqrt{2^m m!}} H_m\left(\frac{v_\parallel}{v_{\text{the}}}\right) g_m(x, y, z, t) F_{0e}(v_\parallel), \qquad (11)$$

where H_m denotes the Hermite polynomial of order m and g_m is its coefficient. Note that $g_0 = g_1 = 0$ because δn_e and $u_{\parallel e}$ have been explicitly separated in the decomposition of δf_e given in equation (2).

Introducing this expansion into equation (9), and choosing a modified Lenard-Bernstein collision operator [21], yields a set of coupled, fluid-like equations for the coefficients of the Hermite polynomials:

$$\frac{dg_m}{dt} + v_{\text{the}}\hat{\boldsymbol{b}} \cdot \nabla \left(\sqrt{\frac{m+1}{2}} g_{m+1} + \sqrt{\frac{m}{2}} g_{m-1} - \delta_{m,1} g_2 \right) =$$

$$-\sqrt{2}\delta_{m,2}\hat{\boldsymbol{b}} \cdot \nabla \frac{e}{cm_e} d_e^2 \nabla_\perp^2 A_\parallel - \nu_{ei}\left(mg_m - 2\delta_{m,2}g_2\right), \qquad (12)$$

where $\delta_{m,2}$ is a Kronecker delta and ν_{ei} is the electron-ion collision frequency. In addition, this choice for $C[g_e]$ defines the resistive diffusivity:

$$\eta \equiv \nu_{ei} d_e^2. \qquad (13)$$

In the Hermite formulation, m is the velocity-space equivalent of k in the usual Fourier representation of position space. Thus, for example, the formation of fine scale structures in velocity space (as arises from phase-mixing) can be conveniently thought of as a transfer of energy to high m's, much in the same

way as the formation of fine scales in real space leads to energy being transferred to high wave numbers k in the usual Fourier representation. On the other hand, the Hermite representation introduces a closure problem, in that the equation for g_m couples to the higher order moment g_{m+1}. We shall see in section 3, however, that a rigorous, nonlinear closure can be obtained.

2.1.2. Reduced MHD limit

The well known reduced MHD (RMHD) equations [27, 28] can be obtained from equations (7–10) by taking the collisional limit $\nu_{ei} \gg \omega$, $k_\perp \ll \left(\rho_i^{-1}, \rho_s^{-1}, d_e^{-1}\right)$, where ω and $k_\perp$ represent the typical frequencies and perpendicular wave numbers of the fluctuations, and $\rho_s = \rho_i/\sqrt{2\tau}$ is the ion sound Larmor radius.

In this limit, the isothermal approximation, $\delta T_{\parallel e} = 0$, applies, and thus equation (9) decouples from equations (7–8). For $k_\perp \rho_i \ll 1$, equation (10) becomes

$$\frac{\delta n_e}{n_{0e}} = \frac{1}{\Omega_i}\nabla_\perp^2 \Phi, \tag{14}$$

where we have defined $\Phi \equiv c\varphi/B_0$ to make contact with the standard terminology. Further defining $A_\parallel \equiv -\sqrt{4\pi n_0 m_i}\Psi$, we obtain:

$$\frac{\partial}{\partial t}\nabla_\perp^2 \Phi + \left[\Phi, \nabla_\perp^2 \Phi\right] \;=\; v_A\frac{\partial}{\partial z}\nabla_\perp^2 \Psi + \left[\Psi, \nabla_\perp^2 \Psi\right], \tag{15}$$

$$\frac{\partial \Psi}{\partial t} + \left[\Phi, \Psi\right] \;=\; \eta\nabla_\perp^2 \Psi + v_A\frac{\partial \Phi}{\partial z}, \tag{16}$$

where v_A is the Alfvén speed based on the guide-field, $v_A = B_0/\sqrt{4\pi n_0 m_i}$.

2.2. Kinetic Reduced Magnetohydrodynamics (KRMHD)

A different set of equations solved by `Viriato` is the Kinetic Reduced Magnetohydrodynamics (KRMHD) model, derived by expanding the gyrokinetic equation in terms of the small parameter $k_\perp \rho_i$ [14]—in this sense, it is the long wavelength limit of gyrokinetics. In this limit, the Alfvénic component of the turbulent fluctuations decouples from the compressive component. The dynamics of the system are completely determined by the Alfvénic fluctuations, which are governed by the reduced MHD equations (15–16). The compressive fluctuations, on the other hand, evolve according to a kinetic equation:

$$\frac{dg}{dt} + v_\parallel \hat{\boldsymbol{b}} \cdot \nabla g \;=\; \frac{v_\parallel F_0}{\Lambda}\hat{\boldsymbol{b}} \cdot \nabla \int dv_\parallel g, \tag{17}$$

where g is related to the perturbed ion distribution function [see equation (183) of Schekochihin et al. [14]] and $F_0 = \exp(-v_\parallel^2/v_{\text{thi}}^2)/\sqrt{\pi}v_{\text{thi}}$ is a one dimensional Maxwellian. The parameter Λ is a linear combination of the physical parameters ion-to-electron temperature ratio, plasma beta, and the ion charge [see equation (182) of Schekochihin et al. [14]].

The structure of Eq. (17) is mathematically similar to that of Eq. (9), the main difference being that this kinetic equation is decoupled from the Alfvénic fluctuations, unlike its KREHM counterpart.

Similar to section 2.1.1, one obtains the following set of equations by expanding Eq. (17) in terms of Hermite polynomials:

$$\frac{dg_0}{dt} + v_{\text{th}i}\nabla_\parallel \frac{g_1}{\sqrt{2}} = 0, \tag{18}$$

$$\frac{dg_1}{dt} + v_{\text{th}i}\nabla_\parallel \left(g_2 + \frac{(1 - 1/\Lambda)}{\sqrt{2}} g_0 \right) = 0, \tag{19}$$

$$\frac{dg_m}{dt} + v_{\text{th}i}\nabla_\parallel \left(\sqrt{\frac{m+1}{2}}\, g_{m+1} + \sqrt{\frac{m}{2}}\, g_{m-1} \right)$$

$$= C[g_m], \quad m \geq 2. \tag{20}$$

Notice that, unlike Eq. (12), equations (18–20) begin at $m = 0$. Additionally, since the term on the right hand side of equation (17) is proportional to the first Hermite polynomial, the parameter Λ makes an appearance only in the equation for g_1.

3. Hermite closure

The Hermite expansion transforms the original electron drift-kinetic equation, (9), into an infinite, coupled set of fluid-like equations, (12) [or, similarly for KRHMD, equation (17) into equations (18–20)]. Formally, the two representations are exactly equivalent, i.e., no information is lost by introducing the Hermite representation. However, the numerical implementation of equations (12) obviously requires some form of truncation, i.e., given a certain number of Hermite moments, M, it is necessary to specify some prescription for g_{M+1}. In other words, as in the derivation of any fluid set of equations, the Hermite expansion introduces a closure problem. Attempts to solve this problem have varied, from simply setting $g_{M+1} = 0$ (e.g., [37, 41, 47, 46]), to polynomial closures in which g_{M+1} is extrapolated from a number of previous moments [40, 47]. Particularly noteworthy is the approach followed by Hammett and co-workers [48, 41, 49, 42, 50] where closures have been carefully designed to rigorously capture the linear Landau damping rates (as well as gyro-radius effects and dominant nonlinearities).

In the system of equations under consideration here, it turns out that an asymptotically exact closure can be obtained in the large M limit. Let us consider that the collision frequency is small but finite. Then, there will be a range of m's for which the collisional term is negligible — one may think of this as the m inertial range: energy is injected into low m's via the coupling with Ohm's law, and cascades (phase-mixes) to higher m's. However, as m increases, a dissipation range is encountered, when the collisional term in equation (12) [or in equation (20)] is no longer subdominant with respect to the other terms. Roughly speaking, in the dissipation range, energy arrives at g_m from g_{m-1} and is mostly dissipated there; only an exponentially smaller fraction is passed on to g_{m+1}. One thus expects that $g_{m+1}/g_m \ll 1$ in the dissipation range, by

definition. The implication of this is that, for $m = M$ in the dissipation range, the dominant balance in the equation for g_{M+1} must be

$$v_{\text{the}}\hat{\boldsymbol{b}} \cdot \nabla \sqrt{\frac{M+1}{2}} g_M \approx -\nu_{ei}(M+1)g_{M+1}. \tag{21}$$

Solving this equation for g_{M+1} yields the sought closure [26, 35]. The equation for g_M therefore becomes:

$$\frac{dg_M}{dt} - \kappa_{\parallel e}\hat{\boldsymbol{b}} \cdot \nabla \left(\hat{\boldsymbol{b}} \cdot \nabla g_M\right) + v_{\text{the}}\hat{\boldsymbol{b}} \cdot \nabla \sqrt{\frac{M}{2}} g_{M-1} = -\nu_{ei}Mg_M, \tag{22}$$

where $\kappa_{\parallel e} \equiv v_{\text{the}}^2/2\nu_{ei}$ is the parallel (Spitzer) thermal diffusivity[2]. It is easy to see how the exact same reasoning leads to the equivalent closure for equation (20).

It can be useful to have an *a priori* estimate of the value of M required to formally justify the asymptotic closure, for a given collision frequency. One such *linear* estimate is provided in Ref. [21]: if the Hermite spectrum is in steady-state, then the collisional cutoff, $m = m_c$, can be shown to occur at[3]:

$$m_c = \left(\frac{3}{2\sqrt{2}}\frac{|k_{\parallel}|v_{\text{the}}}{\nu_{ei}}\right)^{2/3}. \tag{23}$$

Thus, we expect the Hermite closure, equation (21), to be valid if $M \gg m_c$.

The numerical implementation of equation (22) introduces some difficulties and will be discussed in section 6.3.

3.1. Hypercollisions

Since our primary interest lies in weakly collisional plasmas, one finds that $m_c \gg 1$. For example, a simple estimate using standard parameters for the solar corona suggests $m_c \approx 10^4$; certain experiments on JET [25] suggest $m_c \approx 180$ in the edge region, considerably smaller than for the solar corona, but still quite large. Further noticing that such cases are invariably tied to a broad range of spatial scales, thereby also requiring high spatial resolutions, renders obvious the impracticability of such computations: not only must one solve a very large set of nonlinear, coupled PDE's, as also the stiffness increases, due to the coefficients proportional to $\sqrt{m}$. One possibility of avoiding this problem is to artificially enhance the value of the collision frequency. Note however that $m_c \sim \nu_{ei}^{-2/3}$, i.e., a relatively weak scaling, implying that cutting the number of necessary

---

[2]Note that if one wishes to close the system at $M = 2$ (i.e., the semi-collisional limit), then this equation needs to include the term proportional to the electron current [the first term on the RHS of equation (12)], becoming equation (99) of Ref. [21].

[3]This discussion implicitly assumes that one is dealing with a turbulent situation in statistical steady state. Alternatively, one may wish to analyse a linear instability; in that case, another cutoff appears, $m_\gamma = (|k_{\parallel}|v_{\text{the}}/(2\sqrt{2}\gamma)^2$ [21]. If $m_\gamma < m_c$ then the collisional cutoff is superseded. This does not affect any of the considerations drawn here.

m's down to computationally manageable sizes would require drastic increases in the collision frequency. To make matters worse, the collision operator scales only linearly with m, implying that in fact one needs to retain $m \gg m_c$ to adequately capture the dissipation range and validate the closure.

One way to circumvent these difficulties is to make use of a 'hyper-collision' operator, i.e., add a term of the form $-m^h \nu_H g_m$ to the RHS of equation (12). Here, h is the order of the hyper-diffusion operator (a typical value would be $h = 6$) and ν_H is a numerically-based coefficient defined such that energy arriving at $m = M$ can be dissipated in one timestep:

$$\frac{\partial g_M}{\partial t} \sim M^h \nu_H g_M. \tag{24}$$

Thus, in practice, one may simply set [51, 26]:

$$\nu_H = 1/(\Delta t M^h). \tag{25}$$

It is worth remarking that if it is possible to choose a value of M that is very deep into the dissipation range, then presumably the issue of which closure to implement becomes less sensitive, and it may be justified to simply set $g_{M+1} = 0$. Indeed, we have performed simulations with both closures and observed no differences (not reported in this paper).

Finally, we point out that in alternative to a hyper-collision operator one may use a spectral filter (in m-space), such as the one of Hou and Li [52], as proposed by Parker and Dellar [46] (see also section 6.1.1 for a discussion of this filter in Fourier space).

4. Energy

In the absence of collisions, equations (7–9) conserve a quadratic invariant usually referred to as free energy [14]. This quantity can be defined as $W = W_{\text{fluid}} + H_e$, where [21]

$$W_{\text{fluid}} = \sum_{\boldsymbol{k}} \left[1 + \frac{1}{\tau}(1 - \Gamma_0)\right] \frac{1}{\tau}(1 - \Gamma_0) \frac{e^2 n_{0e} |\varphi_{\boldsymbol{k}}|^2}{2T_{0e}} + \int \frac{d^3\boldsymbol{r}}{V} \frac{|\nabla_\perp A_\|\|^2 + d_e^2 |\nabla_\perp^2 A_\|\|^2}{8\pi} \tag{26}$$

is the "fluid" (electromagnetic) part of the free energy, and

$$H_e = \int \frac{d^3\boldsymbol{r}}{V} \int d^3\boldsymbol{v} \frac{T_{0e} g_e^2}{2F_{0e}} \tag{27}$$

is the electron free energy (i.e., the free energy associated with the reduced electron distribution function g_e).

Upon introducing the Hermite expansion of g_e, equation (11), and allowing for finite collisions (modelled by the Lenard-Bernstein collision operator), one finds that W evolves according to the following equation [21]:

$$\frac{d}{dt} W_{\text{fluid}} + \frac{d}{dt} \int \frac{d^3\boldsymbol{r}}{V} \frac{n_{0e} T_{0e}}{2} \sum_{m=2}^{\infty} g_m^2 = -n_{0e} T_{0e} \nu_{ei} \int \frac{d^3\boldsymbol{r}}{V} \sum_{m=3}^{\infty} m g_m^2 - \frac{4\pi}{c^2} \eta \int \frac{d^3\boldsymbol{r}}{V} j_\|^2. \tag{28}$$

The above equation is exact. However, as discussed in section 3, the numerical implementation of the Hermite expansion requires that only a finite number of Hermite polynomials are kept, and some form of closure to the expansion is required. If we adopt the closure described by equation (21), and truncate the expansion at $m = M$, equation (28) adopts the truncated form:

$$\frac{d}{dt}W_{\text{fluid}} + \frac{d}{dt}\int \frac{d^3\boldsymbol{r}}{V}\frac{n_{0e}T_{0e}}{2}\sum_{m=2}^{M}g_m^2 =$$

$$-n_{0e}T_{0e}\nu_{ei}\int \frac{d^3\boldsymbol{r}}{V}\sum_{m=3}^{M}mg_m^2 - n_{0e}T_{0e}\kappa_e\int \frac{d^3\boldsymbol{r}}{V}\left(\hat{\boldsymbol{b}}\cdot\nabla g_M\right)^2 - \frac{4\pi}{c^2}\eta\int \frac{d^3\boldsymbol{r}}{V}j_\parallel^2,$$

(29)

where the second term on the RHS is due to the specific closure that we have used (and would vanish if, for example, we instead use the simpler closure $g_{M+1} = 0$.)

The same arguments that were invoked to motivate the Hermite closure in section 3 apply here to justify the asymptotic equivalence of the full form of the energy balance, equation (28) and its truncated version, equation (29) — that is, as long as M is as large as required for g_M to lie in the collisional (i.e., m-) dissipation range, one expects the terms neglected in going from equation (28) to equation (29) to be exponentially small.

The corresponding equation for KRMHD is equation (4.7) of Ref. [44]. The closure that we propose in section 3 can be implemented in this set of equations in a similar way, and it is straightforward to obtain the KRMHD counterpart of equation (29).

5. Normalizations

The normalizations that we adopt for the KREHM set of equations (7,8,10,12) are:

- *Length scales:*

$$(\hat{x}, \hat{y}) = (x, y)/L_\perp; \quad \hat{z} = z/L_\parallel,$$

(30)

where $L_\perp$, $L_\parallel$ are, respectively, the perpendicular and parallel (to the guide-field) reference length-scales.

- *Times:*

$$\hat{t} = t/\tau_A,$$

(31)

where $\tau_A = L_\parallel/v_A$ is the parallel Alfvén time.

- *Fields:*

$$(\hat{n}_e, \hat{g}_m) = \tau_A \Omega_i \left(\frac{\delta n_e}{n_{0e}}, g_m \right), \tag{32}$$

$$\hat{\varphi} = \frac{c}{B_0} \frac{\tau_A}{L_\perp^2} \varphi, \tag{33}$$

$$\hat{A}_\parallel = \frac{L_\parallel}{L_\perp} \frac{A_\parallel}{L_\perp B_0}. \tag{34}$$

Under these normalizations, equations (7), (8) and (12) become:

$$\frac{dn_e}{dt} = \left[A_\parallel, \nabla_\perp^2 A_\parallel \right] - \frac{\partial}{\partial z} \nabla_\perp^2 A_\parallel, \tag{35}$$

$$\frac{d}{dt} \left(A_\parallel - d_e^2 \nabla_\perp^2 A_\parallel \right) = \eta \nabla_\perp^2 A_\parallel + \rho_s^2 \left[n_e + \sqrt{2} g_2, A_\parallel \right]$$
$$- \frac{\partial \varphi}{\partial z} + \rho_s^2 \frac{\partial}{\partial z} \left(n_e + \sqrt{2} g_2 \right), \tag{36}$$

$$\frac{dg_2}{dt} = \sqrt{3} \frac{\rho_s}{d_e} \left\{ \left[A_\parallel, g_3 \right] - \frac{\partial g_3}{\partial z} \right\} + \sqrt{2} \left\{ \left[A_\parallel, \nabla_\perp^2 A_\parallel \right] - \frac{\partial}{\partial z} \nabla_\perp^2 A_\parallel \right\}, \tag{37}$$

$$\frac{dg_m}{dt} = \sqrt{m+1} \frac{\rho_s}{d_e} \left\{ \left[A_\parallel, g_{m+1} \right] - \frac{\partial g_{m+1}}{\partial z} \right\} + \sqrt{m} \frac{\rho_s}{d_e} \left\{ \left[A_\parallel, g_{m-1} \right] - \frac{\partial g_{m-1}}{\partial z} \right\}$$
$$- m \nu_{ei} g_m, \quad m > 2. \tag{38}$$

where now

$$\frac{d}{dt} = \frac{\partial}{\partial t} + \left[\varphi, \ldots \right]. \tag{39}$$

The normalized form of the quasi-neutrality equation (10) is

$$n_e = \frac{2}{\rho_i^2} \left[\hat{\Gamma}_0(\alpha) - 1 \right] \varphi. \tag{40}$$

It can immediately be seen that neglecting the $g's$ reduces the above set of equations to the simpler two-field gyrofluid model treated in [30].

For the KRMHD set of equations (18–20) the normalisation of space and time are as above, upon which the only modification is the conversion of the prefactor v_{thi} into $\sqrt{\beta_i}$, where $\beta_i = 8\pi n_{0i} T_{0i} / B_0^2$ is the ion plasma beta. The normalisation of the Hermite moments g_m is arbitrary since those equations are linear in g_m.

6. Numerical discretization

The RHS of equations (35–38) is conveniently separated into operators acting either in the direction perpendicular (x, y) or parallel (z) to the guide field. This suggests that an efficient way of integrating those equations is to use operator splitting techniques such as to individually handle each class (perpendicular

or parallel) of operators. `Viriato` allows for both Godunov [53] or Strang splitting [54]. Although Godunov splitting is formally only 1st-order accurate, direct comparisons of both splitting schemes performed by us (not reported here) yield undistinguishable results. Thus, by default, `Viriato` employs Godunov splitting (as it is computationally cheaper); all results reported in section 7 are obtained with this option.

We now detail the algorithms employed for the perpendicular and parallel steps.

6.1. Perpendicular direction

The numerical discretisation of equations (35–38) is the straightforward generalisation of that derived in [30][4]. For presentational simplicity, let us denote the nonlinear terms (i.e., the Poisson brackets) in equations (35–38) by generalised operators, such that we have[5]:

$$\frac{\partial n_e}{\partial t} = \mathcal{N}(n_e, A_\parallel), \tag{41}$$

$$(1 + k_\perp^2 d_e^2)\frac{\partial A_\parallel}{\partial t} = \mathcal{A}(n_e, A_\parallel, g_2) - \eta k_\perp^2 (A_\parallel - A_{\parallel,eq}), \tag{42}$$

$$\frac{\partial g_2}{\partial t} = \mathcal{G}_2(n_e, A_\parallel, g_2, g_3), \tag{43}$$

$$\frac{\partial g_m}{\partial t} = \mathcal{G}_m(n_e, A_\parallel, g_{m-1}, g_m, g_{m+1}) - m\nu_{ei}g_m. \tag{44}$$

Then, the integration scheme is as follows. First we take a predictor step:

$$n_e^{n+1,*} = n_e^n + \Delta t \mathcal{N}(n_e^n, A_\parallel^n), \tag{45}$$

$$A_\parallel^{n+1,*} = e^{-D_\eta \Delta t} A_\parallel^n + \left(1 - e^{-D_\eta \Delta t}\right) A_{\parallel,eq} +$$
$$\frac{\Delta t}{2} \frac{1 + e^{-D_\eta \Delta t}}{1 + k_\perp^2 d_e^2} \mathcal{A}(n_e^n, A_\parallel^n, g_2^n), \tag{46}$$

$$g_2^{n+1,*} = g_2^n + \Delta t \mathcal{G}_2(n_e^n, A_\parallel^n, g_2^n, g_3^n), \tag{47}$$

$$g_m^{n+1,*} = e^{-m\nu_{ei}\Delta t} g_m^n +$$
$$\frac{\Delta t}{2} \left(1 + e^{-m\nu_{ei}\Delta t}\right) \mathcal{G}_m(n_e^n, A_\parallel^n, g_{m-1}^n, g_m^n, g_{m+1}^n), \tag{48}$$

---

[4]With the exception that here we do not include the semi-implicit operator that was the main subject of Ref. [30]. Although the semi-implicit operator derived there can easily be extended to the KREHM equations — by using the full kinetic Alfvén wave dispersion relation, equation (76) — this is not the focus of this paper and we prefer to leave it out of the discussion.

[5]We include here also, in Ohm's law, an external electric field $E_{\text{ext}} = -\eta\nabla_\perp^2 A_{\parallel,eq}$ which is used in tearing mode simulations to prevent the resistive diffusion of the background (reconnecting) magnetic field.

where $\mathcal{D}_\eta = k_\perp^2 \eta / (1 + k_\perp^2 d_e^2)$. This is followed by the corrector step, which can be iterated p times until the desired level of convergence is achieved:

$$
\begin{aligned}
A_\parallel^{n+1,p+1} &= e^{-D_\eta \Delta t} A_\parallel^n + \left(1 - e^{-D_\eta \Delta t}\right) A_{\parallel,eq} + \frac{\Delta t}{2} \frac{e^{-D_\eta \Delta t}}{1 + k_\perp^2 d_e^2} \mathcal{A}(n_e^n, A_\parallel^n, g_2^n) + \\
&\quad \frac{\Delta t}{2} \frac{1}{1 + k_\perp^2 d_e^2} \mathcal{A}(n_e^{n+1,p}, A_\parallel^{n+1,p}, g_2^{n+1,p}),
\end{aligned}
\tag{49}
$$

$$
n_e^{n+1,p+1} = n_e^n + \frac{\Delta t}{2} \mathcal{N}\left(n_e^n, A_\parallel^n\right) + \frac{\Delta t}{2} \mathcal{N}\left(n_e^{n+1,p}, A_\parallel^{n+1,p+1}\right),
\tag{50}
$$

$$
\begin{aligned}
g_2^{n+1,p+1} &= g_2^n + \frac{\Delta t}{2} \mathcal{G}\left(n_e^n, A_\parallel^n, g_2^n, g_3^n\right) + \\
&\quad \frac{\Delta t}{2} \mathcal{G}_2(n_e^{n+1,p+1}, A_\parallel^{n+1,p+1}, g_2^{n+1,p}, g_3^{n+1,p}),
\end{aligned}
\tag{51}
$$

$$
\begin{aligned}
g_m^{n+1,p+1} &= e^{-m\nu_{ei}\Delta t} g_m^n + \frac{\Delta t}{2} e^{-m\nu_{ei}\Delta t} \mathcal{G}_m\left(n_e^n, A_\parallel^n, g_{m-1}^n, g_m^n, g_{m+1}^n\right) + \\
&\quad \frac{\Delta t}{2} \mathcal{G}_m\left(n_e^{n+1,p+1}, A_\parallel^{n+1,p+1}, g_{m-1}^{n+1,p+1}, g_m^{n+1,p}, g_{m+1}^{n+1,p}\right).
\end{aligned}
\tag{52}
$$

For presentational simplicity, we have not included here the hyper-diffusion and hyper-collisions operators, but it is trivial to do so: they are handled in the same way as the resistivity or the collisions are in the above equations.

6.1.1. Dealiasing vs. Fourier smoothing

To deal with the possibility of aliasing instability [55], `Viriato` offers two options. One is the standard 2/3's rule [56], where the Fourier transformed fields are multiplied by a step function $\rho(k/k_{max})$ defined by:

$$
\rho(k/k_{max}) = \begin{cases} 1 & \text{if } |k|/k_{max} \le 2/3, \\ 0 & \text{if } |k|/k_{max} > 2/3, \end{cases}
\tag{53}
$$

where $k_{max} = N/2$ for a grid with N points. The second option is the high-order Fourier filter proposed by Hou & Li [52]:

$$
\rho(k/k_{max}) = \exp\left[-36 \left(|k|/k_{max}\right)^{36}\right].
\tag{54}
$$

Compared to equation (53), the Hou-Li filter retains 12-15% more active Fourier modes in each direction. For other advantages of this filter, and justification of its specific functional form, the reader is referred to Ref. [52]. Tests reported in Refs. [52, 57, 58, 59] unanimously confirm the numerical superiority of the Hou-Li filter over the 2/3's rule dealiasing, as will our results presented in section 7.4.

6.2. Parallel direction

`Viriato` has inbuilt two distinct methods for the integration of the equations in the direction along the guide-field, z: a MacCormack scheme [60], and a combination of a third-order total variation diminishing (TVD) Runge Kutta

14

method for the time derivative [33] with a seventh-order upwind discretization for the fluxes [34] (TVDRK3UW7 for short). The MacCormack scheme is fairly standard (see, e.g., [61, 62] for textbook presentations) and there is no need to detail it here. The TVDRK3UW7 is not as conventional and is described below.

6.2.1. Characteristics

The z-advection step consists in solving the following set of equations:

$$\frac{d\mathbf{u}}{dt} = A\frac{d\mathbf{u}}{dz}, \tag{55}$$

where

$$\mathbf{u} = (n_e, A_\parallel, g_2, ..., g_M)^T \tag{56}$$

is the solution vector and A is tridiagonal matrix of size $(M+1) \times (M+1)$ whose only non-zero entries are the coefficients of the z-derivatives, as follows:

$$A_{k,k+1} = \left\{ k_\perp^2, \sqrt{2}\rho_s^2, -\sqrt{3}\frac{\rho_s}{d_e}, \cdots, -\sqrt{m+1}\frac{\rho_s}{d_e}, \cdots \right\},$$
$$k = 1, \cdots, M, \tag{57}$$
$$A_{k,k-1} = \left\{ \frac{1}{1+k_\perp^2 d_e^2}\left(\rho_s^2 - \frac{\rho_i^2}{2(\Gamma_0 - 1)}\right), \sqrt{2}k_\perp^2, -\sqrt{3}\frac{\rho_s}{d_e}, \cdots, -\sqrt{m}\frac{\rho_s}{d_e}, \cdots \right\},$$
$$k = 2, \cdots, M. \tag{58}$$

To be able to use upwind schemes, we need to write equation (55) in characteristics form, i.e., we need to diagonalize A. To do so, we introduce the matrix P such that equation (55) becomes

$$P^{-1}\frac{d\mathbf{u}}{dt} = P^{-1}APP^{-1}\frac{d\mathbf{u}}{dz}. \tag{59}$$

We define $\mathbf{w} \equiv P^{-1}\mathbf{u}$ and solve for P requiring that

$$P^{-1}AP = D, \tag{60}$$

where D is a diagonal matrix. The equation for $\mathbf{w}$ is now in characteristics form:

$$\frac{d\mathbf{w}}{dt} = D\frac{d\mathbf{w}}{dz}, \tag{61}$$

namely, if $D(j) > 0$, w_j is a right propagating wave field, and vice-versa. Finally, since the entries of A are independent of z, so are the entries of D. Equation (61) can thus be written in flux-conservative form:

$$\frac{d\mathbf{w}}{dt} = \frac{d\mathbf{F}}{dz}, \tag{62}$$

where $\mathbf{F} \equiv D\mathbf{w}$.

As is well known from standard linear algebra, the diagonal entries of the matrix D are the eigenvalues of A, whereas P is the matrix whose column vectors

are the eigenvectors of A. In `Viriato`, both eigenvalues and eigenvectors of A are easily obtained with the linear algebra package LAPACK [63].

As an example, let us consider the simplest possible case: the reduced-MHD limit. Matrix A becomes:

$$A = \begin{bmatrix} 0 & k_\perp^2 \\ \frac{1}{k_\perp^2} & 0 \end{bmatrix}. \tag{63}$$

It is a trivial exercise to obtain the matrices P, P^{-1} and D. They are:

$$P = \begin{bmatrix} -k_\perp^2 & k_\perp^2 \\ 1 & 1 \end{bmatrix}, \quad P^{-1} = \begin{bmatrix} -\frac{1}{2k_\perp^2} & \frac{1}{2} \\ \frac{1}{2k_\perp^2} & \frac{1}{2} \end{bmatrix}, \quad D = \begin{bmatrix} -1 & 0 \\ 0 & 1 \end{bmatrix}. \tag{64}$$

In this case, the characteristic fields are

$$\mathbf{w} = P^{-1}\mathbf{u} = \frac{1}{2}(A_\parallel - \frac{n_e}{k_\perp^2}, A_\parallel + \frac{n_e}{k_\perp^2})^T. \tag{65}$$

To relate this to a more familiar case, note that, using equation (40) in the $k_\perp \rho_i \ll 1$ limit to express the electron density perturbation in terms of the electrostatic potential, $n_e = -k_\perp^2 \varphi$, we immediately recognize the commonly used Elsasser potentials:

$$w^\pm = \frac{1}{2}(A_\parallel \pm \varphi). \tag{66}$$

Note that the entries of A are constants, independent of either time or space. Thus, the matrices P, P^{-1} and D need only to be calculated once per run, with negligible impact on the overall code performance.

6.2.2. Fluxes

The derivative of the flux $\mathbf{F}$ is computed using a seventh-order upwind scheme [34]:

$$\left(\frac{d\mathbf{F}}{dz}\right)_i = \frac{\mathbf{F}_{i+1/2} - \mathbf{F}_{i-1/2}}{\Delta z}, \tag{67}$$

where, for the jth component of $\mathbf{F}$, we have

$$F_{i+1/2}^j = -\frac{1}{140}F_{i+4}^j + \frac{5}{84}F_{i+3}^j - \frac{101}{420}F_{i+2}^j + \frac{319}{420}F_{i+1}^j$$
$$+\frac{107}{210}F_i^j - \frac{19}{210}F_{i-1}^j + \frac{1}{105}F_{i-2}^j, \quad D_j > 0, \tag{68}$$

$$F_{i+1/2}^j = -\frac{1}{140}F_{i-3}^j + \frac{5}{84}F_{i-2}^j - \frac{101}{420}F_{i-1}^j + \frac{319}{420}F_i^j$$
$$+\frac{107}{210}F_{i+1}^j - \frac{19}{210}F_{i+2}^j + \frac{1}{105}F_{i+3}^j, \quad D_j < 0. \tag{69}$$

16

6.2.3. Time derivative

For the time integration of equation (62) we follow [64]. The time derivative is discretized using an optimal third-order total variation diminishing (TVD) Runge Kutta method [33]:

$$
\begin{aligned}
\mathbf{w}^{(1)} &= \mathbf{w}^{(n)} + \Delta t \frac{d\mathbf{F}^{(n)}}{dz}, \\
\mathbf{w}^{(2)} &= \frac{3}{4}\mathbf{w}^{(n)} + \frac{1}{4}\mathbf{w}^{(1)} + \frac{1}{4}\Delta t \frac{d\mathbf{F}^{(1)}}{dz}, \\
\mathbf{w}^{(n+1)} &= \frac{1}{3}\mathbf{w}^{(n)} + \frac{2}{3}\mathbf{w}^{(2)} + \frac{2}{3}\Delta t \frac{d\mathbf{F}^{(2)}}{dz}.
\end{aligned}
\tag{70}
$$

The final step is to compute $\mathbf{u}^{(n+1)} = P\mathbf{w}^{(n+1)}$.

Compared to the MacCormack method, the TVDRK3UW7 scheme just described has the disadvantage of being somewhat slower, as it requires three evaluations of the right hand side (as opposed to only two for MacCormack) and there are more communications involved between different processors to compute the fluxes, equations (68–69). This is partially offset by the fact that the TVDRK3UW7 scheme requires much fewer grid points per wavelength than the MacCormack method for an adequate resolution, as will be exemplified in section 7.1.

6.3. Numerical implementation of the Hermite closure

Expanding the $\hat{\boldsymbol{b}} \cdot \nabla$ operator in the closure term in equation (22), we find that it becomes:

$$
\begin{aligned}
\frac{dg_M}{dt} &= -v_{\mathrm{the}}\hat{\boldsymbol{b}} \cdot \nabla \sqrt{\frac{M}{2}} g_{M-1} \\
&+\kappa_{\|e}\left\{\frac{\partial^2 g_M}{\partial z^2} - \frac{1}{B_0}\frac{\partial}{\partial z}\left[A_\|, g_M\right] - \frac{1}{B_0}\left[A_\|, \frac{\partial g_M}{\partial z}\right] + \frac{1}{B_0^2}\left[A_\|, \left[A_\|, g_M\right]\right]\right\} \\
&-\nu_{ei}Mg_M.
\end{aligned}
\tag{71}
$$

As we have discussed in previous sections, the numerical algorithm employed in `Viriato` uses operator splitting methods to deal separately with the z-derivatives and with the Poisson brackets (i.e., it splits the dynamics parallel and perpendicular to the magnetic guide-field). This raises a difficulty when discretising the equation above, which contains mixed terms (the second and third terms inside the curly brackets) introduced by the closure, equation (21); this is an especially subtle issue when the z-step scheme advects the equations in characteristics form, as is the case of the TVDRK3UW7 that we employ (and would equally be the case for any other upwind scheme).

Simple solutions to this problem require abandoning the operator splitting scheme and forsaking the use of the characteristics form for the z-derivative terms of the equations, both of which are not only highly convenient from the point of view of numerical accuracy and stability, but also physically motivated.

One possibility would be to treat this equation differently from all other equations solved by the code. Although this is certainly possible, at this stage we have chosen not to introduce this additional complexity. As such, the actual form of equation (71) implemented in `Viriato` is

$$\frac{dg_M}{dt} = -v_{\text{th}e}\hat{\boldsymbol{b}} \cdot \nabla \sqrt{\frac{M}{2}} g_{M-1} + \kappa_{\|e} \left\{ \frac{\partial^2 g_M}{\partial z^2} + \frac{1}{B_0^2} \left[A_\|, [A_\|, g_M]] \right] \right\}$$
$$-\nu_{ei} M g_M. \tag{72}$$

We emphasize that the dropping of the mixed terms is purely for algorithmic reasons. From the physical point of view those terms are, *a priori*, as important as the closure terms which are kept; their implementation is thus left to future work. A serious drawback of this approach, for example, is that the semi-collisional limit of the KREHM equations (which results from setting $M = 2$, see Section V.C of Ref. [21]) is, therefore, not correctly captured.

On the other hand, note that: (i) for 2D problems, our implementation of the closure is exact; (ii) for simple linear 3D problems [where the background magnetic field is simply given by that guide-field (which is the setup used to investigate Alfvén wave propagation in section 7.2), the numerical implementation of the closure is also exact; (iii) in weakly collisional plasmas (which are our main focus), provided that M is sufficiently large to lie in the collisional dissipation range, one expects $g_{M+1} \ll g_M$ and thus the actual functional form of the closure may not be very important; (iv) if we first apply the operator splitting scheme (i.e., the separation of the perpendicular and parallel operators) and then impose our closure scheme on the parallel and perpendicular equations separately, we would obtain equation (72) instead of equation (71).

Finally, we remark that adopting equation (72) as the evolution equation for g_M changes the second term on the RHS of the energy balance equation, (29), in the obvious way.

7. Numerical tests

In this section, we report an extensive suite of linear and nonlinear benchmarks of `Viriato`.

7.1. Comparison of the MacCormack and the TVDRK3UW7 methods

To illustrate the relative merits of the two numerical schemes for the z-advection available in `Viriato`, we carry out a simple test in the limit of isothermal electrons and cold ions. Equations (35–38) and equation (40) reduce to

$$\frac{\partial n_e}{\partial t} = k_\perp^2 \frac{\partial A_\|}{\partial z}, \tag{73}$$

$$\frac{\partial A_\|}{\partial t} = \frac{1}{k_\perp^2} \frac{1 + k_\perp^2 \rho_s^2}{1 + k_\perp^2 d_e^2} \frac{\partial n_e}{\partial z}. \tag{74}$$
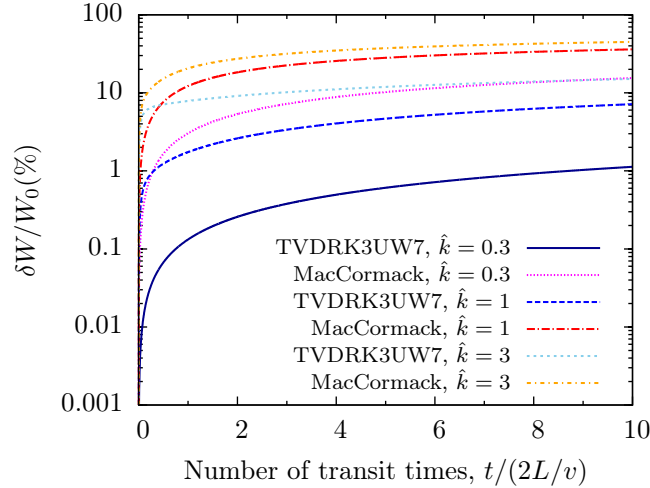
Figure 1: Energy conservation for the MacCormack and the TVDRK3UW7 schemes for the linear advection test problem defined in Equations (73–74). The x-axis is the time normalized by the transit time across the simulation box, $2L/v$. The y-axis is the variation in energy (δW) normalized by the initial energy, W_0. The parameter $\hat{k} = k\Delta z = 2\pi/n_p$, where n_p is the number of grid points per wavelength.

The initial condition we adopt is:

$$A_\parallel(z, t = 0) = \frac{\tanh\left[k(z + 0.25)\right] + \tanh\left[k(z - 0.25)\right]}{2}. \tag{75}$$

Equations (73–74) are solved on a periodic box $-L \leq z \leq L$, with $L = \pi$. The grid step size is $\Delta z = 2L/64$. The time step is set by the CFL condition $\Delta t = 0.25\Delta z/v$, where $v = \sqrt{(1 + k_\perp^2 \rho_s^2)/(1 + k_\perp^2 d_e^2)}$. We chose $k_\perp = 1$, $\rho_s = 1$ and $d_e = 0.01$. There is no explicit dissipation in this test.

A measure of how well resolved the wave front is is given by the parameter $\hat{k} = k\Delta z = 2\pi/n_p$, where n_p is the number of grid points per wavelength. We test the behaviour of the MacCormack and TVDRK3UW7 schemes for three representative values of $\hat{k} = 0.3,\ 1,\ 3$ (note that the highest resolvable wave number corresponds to $n_p = 2$, i.e., $\hat{k} = \pi$). For each of these cases, the equations are integrated for 10 transit times across the box, $t_{\text{transit}} = 2L/v$.

Time traces of the energy conservation for both schemes are plotted in Figure 1. As expected, the TVDRK3UW7 scheme behaves remarkably better than MacCormack. Notice, for example, that for the extreme case of $\hat{k} = 3$, TVDRK3UW7 yields an amount of energy loss after 10 crossing times of $\sim 15\%$, very similar to what is obtained with the MacCormack scheme for the ten times better resolved case of $\hat{k} = 0.3$.

Besides much better energy conservation properties, we find the TVDRK3UW7 scheme to be very robust against spurious Gibbs oscillations, even though it is not a shock-capturing scheme. This is clearly visible in Figure 2, where we plot
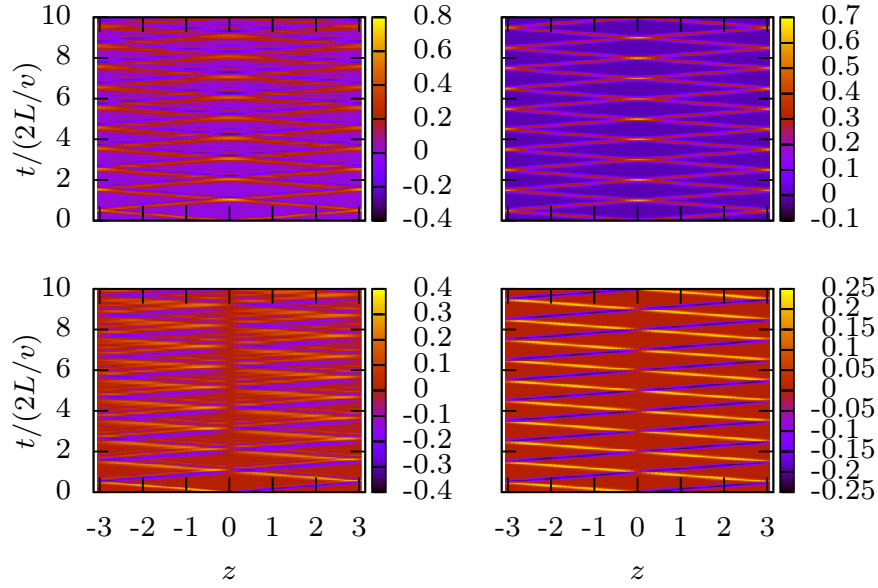
Figure 2: Results from the linear advection test problem of section 7.1. Contour plots of the time evolution of $A_\parallel$ (top) and n_e (bottom) using the MacCormack scheme (left panels) and the TVDRK3UW7 scheme (right panels), for the case $\hat{k} = 1$. The MacCormack scheme is seen to introduce strong Gibbs oscillations, which are remarkably minimized by the TVDRK3UW7 scheme.
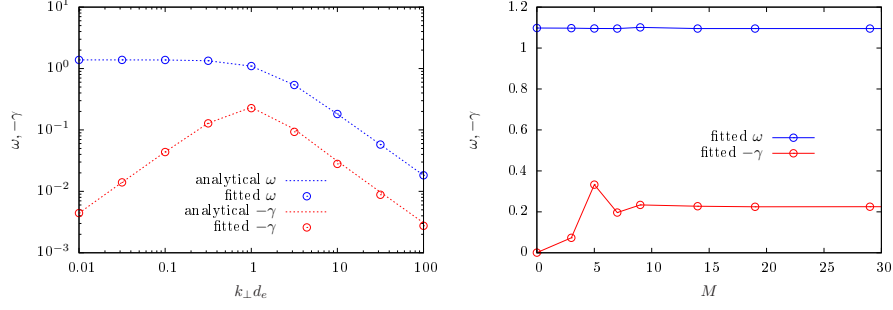
Figure 3: Left: Frequency and damping rate of the kinetic Alfvén wave (KAW), in units of τ_A, at fixed $k_\perp \rho_i = 1$, $\tau = 1$, $M = 19$, as a function of the electron skin-depth $d_e = c/\omega_{pe}$. Lines are the exact solution of the analytical dispersion relation, equation (76), whereas data points are obtained from `Viriato`. Right: KAW frequency and damping rate obtained from `Viriato` for fixed $k_\perp d_e = 1$, as a function of the total number of Hermite moments kept, M.

the time history of the profiles of $A_\parallel$ and n_e obtained with both schemes for $\hat{k} = 1$. As can be seen, the TVDRK3UW7 scheme advects the initial condition with no visible deterioration, unlike the MacCormack scheme.

7.2. Linear Kinetic Alfvén Wave

The linearisation of equations (7–9) in the collisionless limit yields the kinetic Alfvén wave dispersion relation [21]:

$$\left[\zeta^2 - \frac{\tau}{Z} \frac{k_\perp^2 d_e^2/2}{1 - \Gamma_0(k_\perp^2 \rho_i^2/2)} \right] [1 + \zeta Z(\zeta)] = \frac{1}{2} k_\perp^2 d_e^2, \tag{76}$$

where $\zeta = \omega/|k_\parallel|v_{the}$, $Z(\zeta)$ is the plasma dispersion function and $k_\perp^2 = k_x^2 + k_y^2$.

On the left plot of Figure 3 we show a comparison between the analytical values of the frequencies and damping rates, obtained by solving equation (76), and those computed by `Viriato` setting the number of Hermite moments to $M = 19$ and the number of grid points in the z-direction to 32. Very good agreement is observed over several orders of magnitude of the electron skin depth, d_e; the maximum relative error, obtained for the highest value of d_e, is only a few percent. The right plot shows the values of the frequency and damping rate for $k_\perp d_e = 1$ as a function of the number of Hermite moments. For $M \geq 9$ the damping rate converges to the analytical value ($-\gamma = 0.2331$), whereas for ω very little dependence on M is observed.

7.3. Tearing Mode

The tearing mode [65] is a fundamental plasma instability driven by a background current gradient. Tearing leads to the opening, growth and saturation of (one or more) magnetic island(s) via the reconnection of a background magnetic field. It is of intrinsic interest to magnetic confinement fusion devices, where it occurs either in standard or modified form (i.e., neoclassical tearing,
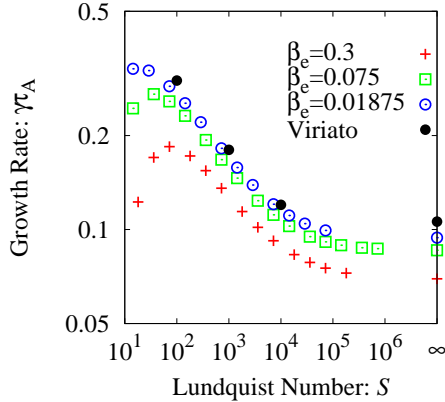
21

Figure 4: Tearing mode growth rate as a function of the Lundquist number. Figure shows a comparison between the results obtained with the gyrokinetic code `AstroGK` [66] for varying values of β_e and `Viriato`. As expected, good agreement is obtained in the small β_e limit.

microtearing). It also represents the most basic paradigm for studies of magnetic reconnection.

In this section, we present the results of a linear benchmark of `Viriato` against the gyrokinetic code `AstroGK` [66] for the tearing mode problem. We consider an in-plane magnetic equilibrium configuration given by $B_{y,eq} = -dA_{\parallel,eq}/dx$, with $A_{\parallel,eq} = A_{\parallel 0}/\cosh^2(x/a)$, with a the normalizing equilibrium scale length. The simulations are performed in a doubly periodic box of dimensions $L_x \times L_y$, with $L_x/a = 2\pi$ and $L_y = 2.5\pi$, such that $\hat{k}_y = 2\pi a/L_y$ yields the tearing instability parameter $\Delta'a = 2(5 - \hat{k}_y^2)(3 + \hat{k}_y^2)/(\hat{k}_y^2\sqrt{4 + \hat{k}_y^2}) \approx 23$. Other parameters are $\rho_i/a = 0.2$, $\tau = 1$, $d_e/a = 0.037$. All `Viriato` simulations keep $M = 10$.

Figure 4 shows a plot of the linear growth rate of the tearing mode as a function of the Lundquist number $S = av_A/\eta$. The $S = \infty$ case is obtained by setting $\eta = 0$, in which case the tearing mode is collisionless, i.e., the frozen-flux condition is broken by electron inertia instead. Calculations with `AstroGK` are done at three different values of β_e and mass ratio: $(\beta_e, m_e/m_i) = (0.3, 0.01)$, $(0.075, 0.0025)$, $(0.01875, 6.25 \times 10^{-4})$ (crosses, squares and circles, respectively; this is the same data as plotted in Fig. 2 of Ref. [18]). As seen, the agreement between the two codes improves for smaller β_e, and is rather good for the smallest value of $\beta_e = 0.01875$. Though it is expected that gyrokinetics will converge to KREHM as β_e is decreased, we note that, at least in this particular case, agreement is achieved for β_e substantially larger than m_e/m_i (a factor of 30), suggesting that KREHM may remain a reasonable approximation to the plasma dynamics outside its strict asymptotic limit of validity set by the requirement $\beta_e \sim m_e/m_i$.

A nonlinear benchmark is provided by the comparison of the tearing mode saturation amplitude with the prediction of MHD theory [67, 68, 69]. This was

Run	Dim.	#Gridpoints	ρ_i/a	Dealiasing	Hyper-diss.?
A	2D	2048^2	0	2/3's rule	no
A1	2D	2048^2	0	2/3's rule	yes
B	2D	2048^2	0	Hou-Li	no
B1	2D	2048^2	0	Hou-Li	yes
C	3D	512^3	0	Hou-Li	yes
D	3D	256^3	2	Hou-Li	yes
E	3+1D	256^3	2	Hou-Li	yes

Table 1: Main parameters for decaying turbulence runs [with the Orszag-Tang-type initial conditions of equations (77–78) for the 2D runs, and of equations (81–82) for the 3D runs]. In all cases, $\rho_s = \rho_i$ and $d_e = 0$. Run E also includes 20 Hermite moments.

reported in Ref. [26], where it is shown that `Viriato` accurately reproduces the theoretical prediction in the parameter region where such prediction is valid [i.e., for $\Delta'a \sim 1$ and as long as islands are larger than the kinetic scales of the problem (ρ_i, ρ_s, d_e)].

Finally, see also Figs. 1 and 3 of Ref. [70] for more direct comparisons between `Viriato` and `AstroGK` in the linear and nonlinear regime of a collisionless tearing mode simulation.

7.4. Orszag-Tang vortex problem

The Orszag-Tang (OT) vortex problem [71] is a standard nonlinear test for fluid codes, and a basic paradigm in investigations of decaying MHD turbulence [71, 72, 73, 74]. Here we present results from a series of 2D and 3D runs, including a kinetic case. For easy reference, we summarise the main parameters of each simulation performed in Table 1.

7.4.1. 2D simulations of the OT vortex problem

To avoid an overly symmetric initial configuration, we adopt the modification of OT initial conditions proposed in Ref. [72], namely[6]:

$$\Phi(x,y) = \cos(2\pi x/L_x + 1.4) + \cos(2\pi y/L_y + 0.5), \tag{77}$$

$$\Psi(x,y) = \cos(4\pi x/L_x + 2.3) + \cos(2\pi y/L_y + 4.1). \tag{78}$$

The runs are performed on a box of dimensions $L_x = L_y = 2\pi$, at a resolution of $N_x \times N_y = 2048^2$ collocation points. In the cases where no hyper-dissipation is used (runs A and B), the resistivity is set to $\eta = 10^{-3}$, and the magnetic Prandtl number $Pm = \nu/\eta = 1$. The kinetic scales ρ_i, ρ_s, d_e are set to zero, so this is strictly a RMHD run.

---

[6]We note for completeness that we have also performed a simulation with the same (symmetric) initial condition as used in Ref. [66] and obtained excellent agreement with the results reported there.
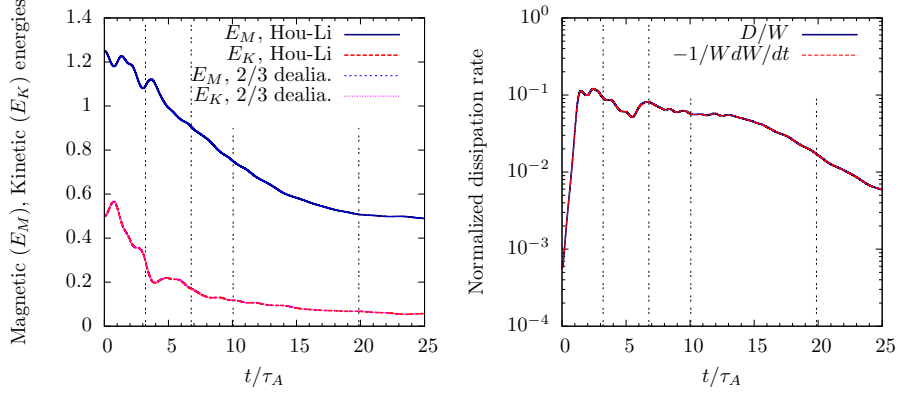
Figure 5: Runs A and B. Left panel: Time traces of the magnetic (E_M) and kinetic (E_k) energies, obtained from runs with different dealiasing methods: "Hou-Li" uses the high-order Fourier filter of Ref. [52], given by equation (54); "2/3 dealia." uses the usual 2/3's rule of Ref. [56], equation (53). Right panel: Time trace of the energy dissipation rate (for the Hou-Li run), normalized by the instantaneous total energy, D/W. Overplotted is $-1/W\,dW/dt$: code conserves energy to better than 0.1% in this run. The vertical dotted lines identify the times at which the contours of Figure 6 and spectra of Figure 7 are plotted.

Magnetic (E_M) and kinetic (E_K) energy time traces for runs A and B are shown on the left-hand panel of Figure 5. We compare the results obtained using the Hou-Li high order Fourier filter, equation (54), with those obtained with the standard 2/3's dealiasing rule of Orszag [56], equation (53). The agreement between the two sets of results is perfect, demonstrating that the Hou-Li filter does as good a job at conserving energy as the 2/3's rule.

The right-hand panel shows the time trace of the energy dissipation, normalized by the instantaneous total energy, i.e.,

$$\frac{D}{W} \equiv \frac{\int dV(\eta j^2 + \nu \omega^2)}{\frac{1}{2}\int dV(B^2 + u^2)}. \tag{79}$$

Since no energy is being injected into the system, the RMHD equations should obey the conservation relation

$$\frac{dW}{dt} = -D. \tag{80}$$

In order to demonstrate the accuracy of the code, we overplot a time trace of $-1/W\,dW/dt$. The very good agreement between the two curves is manifest; in this particular run, equation (80) is satisfied to better than 0.1%.

Contour plots of current and vorticity (i.e., $\nabla_\perp^2 \Phi$) at the times identified by the vertical lines in Figure 5 are plotted in Figure 6 (top and bottom rows, respectively). The formation of sharp current and vorticy sheets is observed, as expected. At $t/\tau_A = 10.0$ one can observe a plasmoid [75, 76] erupting from the current sheet on the lower right-hand corner of the plot, in what is perhaps
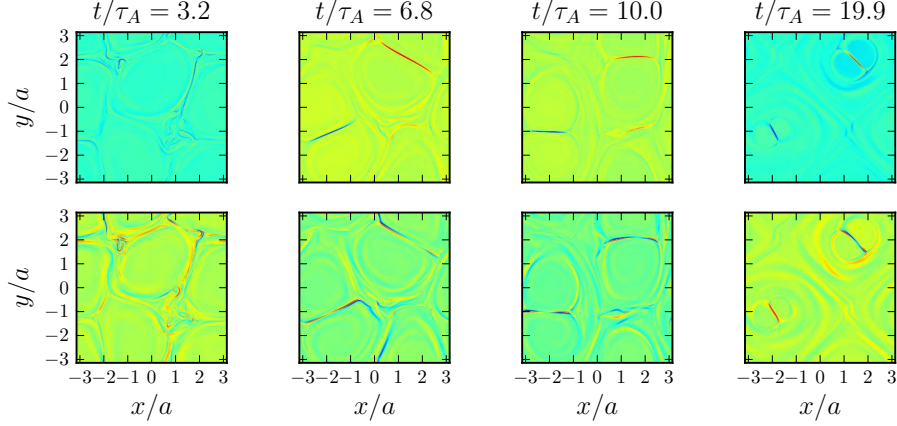
24

Figure 6: Run B (2D). Contour plots of current (top row) and vorticity (bottom row) at different times (identified by the vertical lines in Figure 5).

the small-scale version of the observations reported in Ref. [77]. The role of the tearing instability of current sheets in 2D decaying turbulence has been previously discussed in Refs. [72, 74].

Figure 7 shows the total energy spectra obtained from the simulation with the Hou-Li filter (run B), taken at the times identified by the vertical lines in Figure 5. There is no evidence of pile-up (bottleneck) at the small scales (we note that the only dissipation terms present in this simulation are the standard laplacian resistivity and viscosity, i.e., there is no hyper-dissipation). Due to the relatively large values of the dissipation coefficients used in this simulation, the inertial range is very limited and it is not possible to clearly fit a unique power law; for reference, $k_\perp^{-3/2}$ is indicated in Figure 7, following the Iroshnikov-Kraichnan prediction [78, 79], and its numerical confirmation reported in Refs. [72, 74] (although steeper power-laws $\sim k_\perp^{-5/2}$ have also been reported in the literature [80, 59]).

A much longer and cleaner inertial range is obtained by replacing the standard (laplacian) dissipation terms with hyper-dissipation (runs A1 and B1). In that case, the spectra shown in Figure 8 are obtained; the inertial range now shows an excellent agreement with the power-law slope of $-3/2$. Note also the extended inertial range obtained when the Hou-Li filter is used (B1) instead of the standard 2/3's dealiasing.

7.4.2. 3D simulations of the OT vortex problem

For the 3D simulations the initial conditions differ from the 2D case only in that they are modulated in the z-direction, as follows:

$$\Phi(x,y) = [\cos(2\pi x/L_x + 1.4) + \cos(2\pi y/L_y + 0.5)]\sin(2\pi z/L_z), \quad (81)$$

$$\Psi(x,y) = [\cos(4\pi x/L_x + 2.3) + \cos(2\pi y/L_y + 4.1)]\cos(2\pi z/L_z). \quad (82)$$

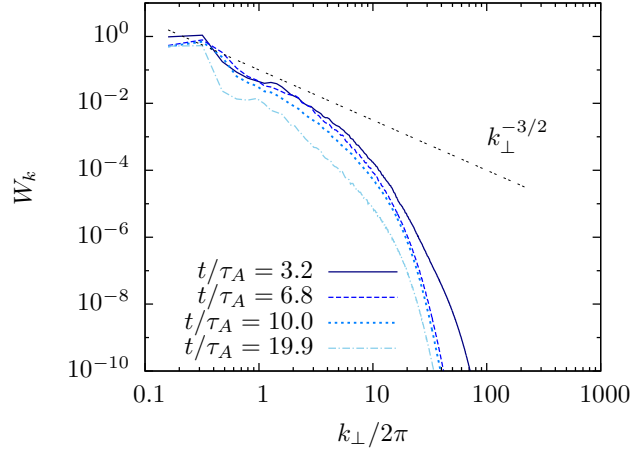Figure 7: Run B (2D). Total energy spectra at different times (identified by the vertical lines in Figure 5). A $k_\perp^{-3/2}$ slope is shown for reference.
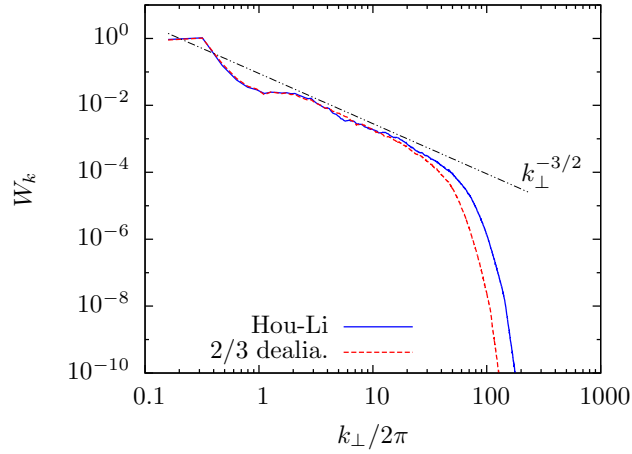

Figure 8: Runs A1 and B1 (2D). Total energy spectra at $t/\tau_A \approx 6.0$ obtained with the Hou-Li filter (blue, full line) and with the standard 2/3's dealising rule (red, dashed line). The Hou-Li method results in an extended inertial range for the same number of collocation points, as expected. Neither spectra shows signs of energy pile-up at the small scales. The power-law $k_\perp^{-3/2}$ is indicated for reference.

26
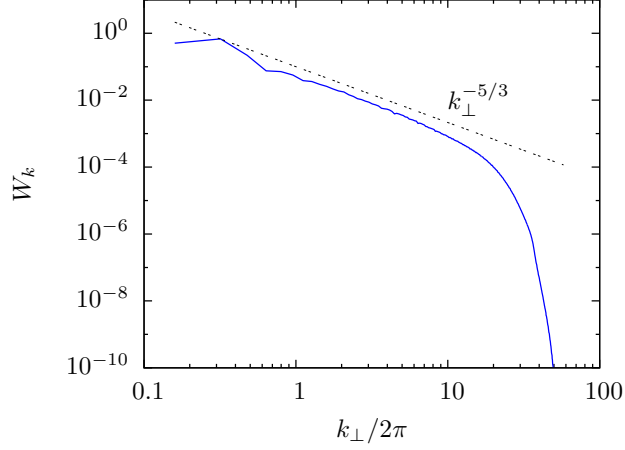
Figure 9: Run C (3D). Total energy spectra at $t/\tau_A \approx 4.0$. A $k_\perp^{-5/3}$ slope is shown for reference.

We perform three different runs with these initial conditions (runs C, D and E). The first (run C) is just a straightforward extension to 3D of run B1, except now with a resolution of $N_x \times N_y \times N_z = 512^3$. The second (run D) is designed to look at sub-ion-Larmor radius turbulence (i.e., kinetic Alfvén wave turbulence); thus we set $\rho_i/a = 2$, $d_e/a = 0.01$, where $a = L_x/(2\pi)$, and $\tau = 1$. The resolution in this case is $N_x \times N_y \times N_z = 256^3$ (we use a smaller resolution here because the timestep, which is set by the CFL condition, is now also smaller, due to the dispersive nature of the kinetic Alfvén waves). Finally, run E also includes the velocity-space dependence, represented with 20 Hermite moments (meaning that it differs from run D in that the electrons are no longer isothermal, i.e., $g_e \neq 0$)

The total energy spectrum obtained for run C is shown in Figure 9. The inertial range shows very good agreement with the Goldreich-Sridhar $k^{-5/3}$ power law [81] and again is clean of bottleneck effects.

Figure 10 shows the magnetic, kinetic and electric energy spectra for run D, where we are now focussing on sub-ion Larmor radius scales. The slopes indicated refer to several power laws that have been widely discussed in the literature. In particular, we see that the separation between electric and magnetic energy scalings, occurring at around $(k_\perp/2\pi)\rho_i \sim 1$, agrees quite well with the solar wind observations reported by Bale *et al.* [82] and with the gyrokinetic simulations of Howes *et al.* [13]. However, instead of the $-7/3$ power law for the magnetic energy suggested in those works (discussed in more detail in Ref. [14]), we see that our data seems to more closely fit a $-8/3$ scaling, which is a better fit to the -2.8 slope often reported in observations (e.g., [83]) and in agreement with the recent work of Boldyrev and Perez [84] on strong kinetic Alfvénic turbulence.
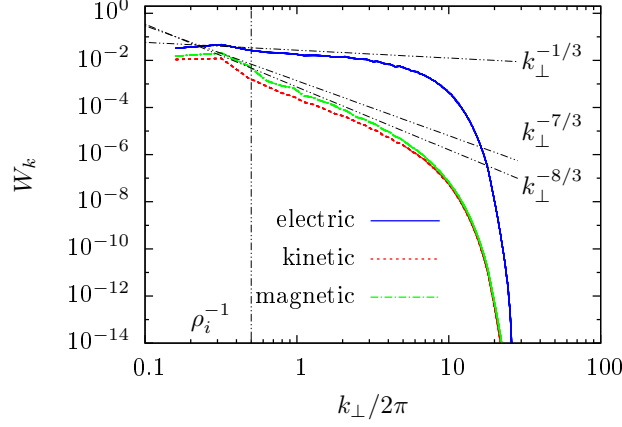
27

Figure 10: Run D (3D). Spectra for decaying turbulence [with OT-like initial conditions, equations (81–82)] at $t/\tau_A \approx 2.2$. The blue (full) line represents the perpendicular electric energy spectrum; the red (dashed) line is the perpendicular magnetic field energy and the green (dash-dot) line is the kinetic energy. The slopes $k_\perp^{-1/3}$, $k_\perp^{-7/3}$ and $k_\perp^{-8/3}$ are indicated for reference (see text for discussion). The vertical line indicates the ion Larmor radius scale.
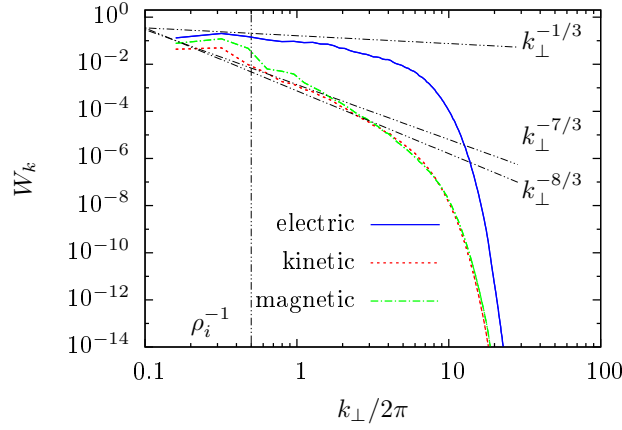

Figure 11: Run E (3D, with 20 Hermite moments). Spectra at $t/\tau_A \approx 2.2$ for OT-decaying kinetic turbulence. Lines represent the same quantities as in Figure 10. See text for a discussion of the power laws indicated.
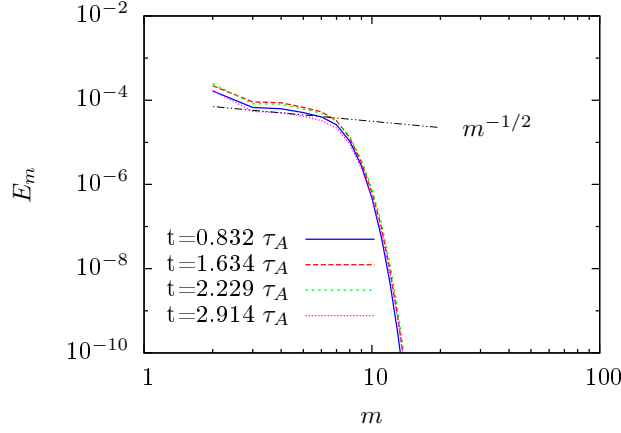
Figure 12: Run E (3D, with 20 Hermite moments). Electron free-energy spectra $E_m = |g_m^2/2|$ at different times. An indicative power law of $m^{-1/2}$ for the inertial range is also shown [21].

Figure 11 again shows energy spectra, this time for run E, which differs from run D in that it also includes Hermite moments (i.e., it is a fully kinetic run, whereas D assumes isothermal electrons, $g_e = 0$). Comparing the magnetic spectra in the two cases (i.e, runs D and E, both drawn at the same time), we see that its values increase at the larger (spatial) scales when adding the Hermite moments, by about an order of magnitude, and run E's spectrum seems to be somewhat steeper than $-8/3$. Such differences may be due to Landau damping, which is present in run E, but absent in run D. The Hermite spectrum (i.e., the electron free energy spectrum, $E_m = |g_m^2|/2$) for run E is shown in Figure 12, at different times. A $-1/2$ slope is indicated for reference; this is the inertial-range slope predicted by Zocco & Schekochihin [21] for the linear phase-mixing of Kinetic Alfvén waves. Since the number of Hermite moments (20) used is quite small we get an equivalently limited inertial range, and thus the agreement with the $-1/2$ slope can only be regarded as indicative; however, this tentative agreement lends credence to the idea that Landau damping may be playing a significant role in this simulation. A detailed analysis of kinetic turbulence in the KREHM framework and, in particular, of the relative importance of the different energy dissipation mechanisms available, will be the subject of a future publication.

Finally, for completeness we show in Figure 13 contour plots of the electron parallel velocity, $u_{e\parallel}$, and of the density perturbations, n_e, taken at the same time as the spectra of Figure 11 ($t/\tau_A \approx 2.2$).

7.5. Collisionless damping of slow modes

We turn now to a benchmark of `Viriato`'s implementation of the KRMHD equations. Linearly, slow modes in KRMHD are subject to collisionless damping via the Barnes damping mechanism [85]. An initial perturbation damps at
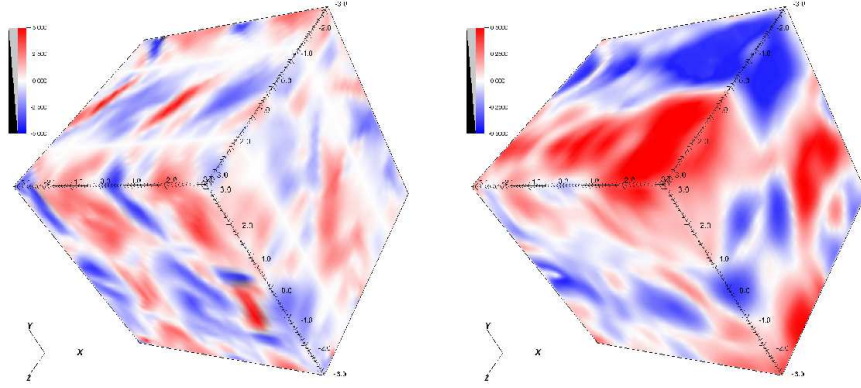
29

Figure 13: Run E: contour plots of the parallel electron velocity, $u_{e\parallel}$ (left), and density perturbations n_e (right), at $t/\tau_A \approx 2.2$.

a rate that depends on the parameter Λ. If slow mode fluctuations are constantly driven with an external force (this is achieved by adding a forcing term to Eq. (17)), then the system can be thought of as a plasma-kinetic Langevin equation. The mean-squared amplitude of the electrostatic potential for such a system reaches a steady-state saturation level, which can be derived analytically [44].

In figure 14, we compare the steady-state saturation levels computed using `Viriato` with the analytical predictions, and the numerical results from another code — `Gandalf` (a fully spectral GPU code that solves the KRMHD equations). Slow mode fluctuations were driven using white noise forcing[7] which injected energy into the system with unit power. The spatial resolution was set to $N_x \times N_y \times N_z = 32^3$; 20 Hermite moments of the distribution function were retained, $M = 20$. The system was evolved until it reached a steady state. The saturation level was then calculated by averaging over the steady state fluctuations for a few Alfvén times. It can be seen that the saturation amplitudes obtained using `Viriato` are in near perfect agreement with those calculated by `Gandalf`, as well as with the analytical prediction.

8. Performance

`Viriato` has been used on a variety of computing clusters, with different architectures. It is quite easy to install and run, having dependencies only on standard, widely-used libraries such as LAPACK [63] and FFTW [87]. Its parallelization relies on standard MPI routines.

---

[7]Another way of forcing the system which is also implemented in `Viriato` is via an oscillating Langevin antenna [86].
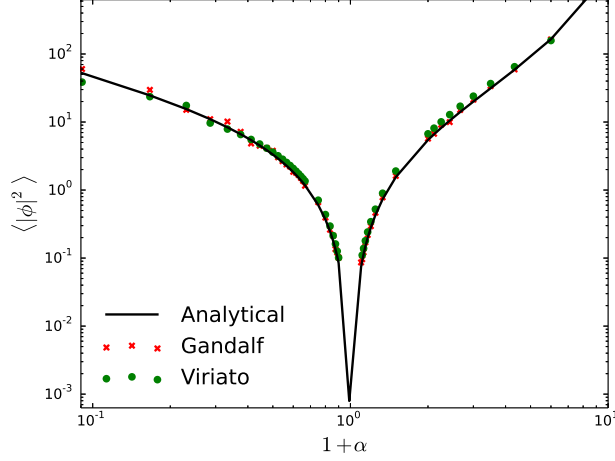
Figure 14: Steady-state amplitude of the electrostatic potential vs $1 + \alpha$, where $\alpha = -1/\Lambda$. The solid line is the analytical prediction [44], the red crosses are numerical results calculated using `Gandalf`, and the green circles are calculated using `Viriato`.

As described in detail in Section 6, the direction parallel to the field can be integrated by two different numerical methods, both of them fairly scalable, in terms of parallel performance. In contrast, the direction perpendicular to $\mathbf{B}_0$ uses standard pseudospectral techniques, which are plagued with well-known limits on scalability, due to the inherent non-locality of Fourier transforms. For this reason, if one wishes to increase the number of processors for a given computation, it is more effective to do so by increasing the ratio between the number of processes for the parallel direction and the number of processes in the perpendicular direction.

The results of such a test, made on the Helios machine (an Intel Xeon E5 cluster), can be seen on Figure 15, where the MacCormack method was used in the parallel direction. The initial conditions are the 3D Orszag-Tang vortex given by equations (81–82), with 15 Hermite moments. We look at strong scaling, keeping the problem size fixed and varying the number of MPI processes, mainly in the parallel direction. This produces a supralinear scaling, which breaks down after 1024 cores for the 256^3 case and at ~ 4096 cores for the 512^3 one. Similar results have been obtained on other clusters, such as Stampede (a mixed Intel Xeon E5 and Intel Xeon Phi Coprocessor cluster), Hopper (a Cray XE6) and Edison (a Cray XC30.

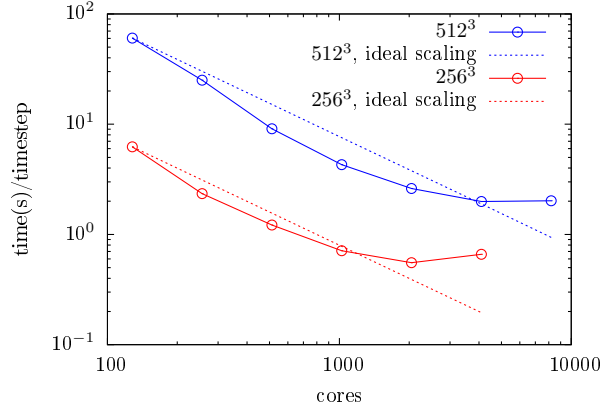Currently ongoing optimization work includes parallelizing the computation of the Hermite moments' via OpenMP.

31

Figure 15: `Viriato` timings measured on the Helios cluster, for two different fixed problem sizes (strong scaling). A supralinear trend can be observed, which breaks down after 1024 cores for the 256^3 case and at ~ 4096 cores for the 512^3 one. The vertical axis gives the wall-clock time (in seconds) spent per timestep.

9. Conclusions

This paper describes `Viriato`, a novel code developed to investigate strongly magnetised, weakly-collisional, fluid-kinetic plasma dynamics in (2D or 3D) slab geometry. `Viriato` solves two different sets of equations: the Kinetic Reduced Electron Heating Model (KREHM) of Zocco & Schekochihin [21] (which simplifies to conventional reduced-MHD [27, 28] in the appropriate limit) and the Kinetic Reduced MHD (KRMHD) equations of Schekochihin *et al.* [14].

The main numerical methods and the overall algorithm are described. A noteworthy feature of `Viriato` is its spectral representation of velocity-space, achieved via a Hermite expansion of the distribution function, as proposed in [21] for KREHM and in [44] for the KRMHD equations. This representation has the attractive property of converting the kinetic equation for the distribution function into a coupled set of fluid-like equations for each Hermite polynomial coefficient — the advantage being that such equations are numerically more convenient to solve than the kinetic equation where they stem from. On the other hand, the Hermite expansion introduces a closure problem (in the sense that the equation for the Hermite coefficient of order m couples to that of order $m+1$). To address this problem, we present a nonlinear, asymptotically rigorous closure whose validity requires only that collisions are finite, but otherwise as small as required. Naturally, the smaller the collision frequency the higher the number of Hermite moments that need to be kept to guarantee the accuracy of the closure. Realistic values of the collision frequency in the systems that are of primary interest to us (e.g., modern fusion devices, space and astrophysical environments) lead to impractically large number of moments. The adoption of a hyper-collision operator (the direct translation into Hermite space of the usual hyper-diffusion operators used in (Fourier) k-space) allows us to deal with

32

this problem. Together with a pseudo-spectral representation of the plane perpendicular to the background magnetic field, and the option of a spectral-like algorithm for the dynamics along the field, the Hermite representation of velocity space implies that `Viriato` is ideally suited to the investigation of magnetised kinetic plasma turbulence and magnetic reconnection, with the unique capability of allowing for the direct monitoring of energy flows in phase-space [26].

A series of linear and nonlinear numerical tests of `Viriato` is presented, with emphasis on Orszag-Tang-type decaying turbulence, both in the fluid and kinetic limits, where it is shown that `Viriato` recovers the theoretically expected power-law spectra. In this context, an interesting, novel result that warrants further investigation and will be discussed in a separate publication is the $\sim m^{-1/2}$ velocity-space (Hermite) spectrum that is obtained in the 3D kinetic (sub-ion Larmor radius scales) Orszag-Tang run presented in section 7.4.2 (see Figure 12). This particular form of the Hermite spectrum is indicative of linear phase mixing [21, 26] and suggests that this (and ensuing Landau damping) may be a key energy transfer mechanism in kinetic decaying turbulence.

Acknowledgements

Appendix A: Addition of a background electron temperature gradient

A recent paper by Zocco *et al.* [35] extends the KREHM model to include a background electron temperature gradient. This extension is also implemented in `Viriato`; results of ongoing investigations exploring different instabilities introduced by these terms (namely, the electron temperature gradient mode, and the microtearing instability) will be reported elsewhere. For completeness, we write below the KREHM equations with this extension in normalised form (see

section 5 for the details of the normalisation adopted in `Viriato`). They are:

$$\frac{dn_e}{dt} = \left[A_\parallel, \nabla_\perp^2 A_\parallel\right] - \frac{\partial}{\partial z}\nabla_\perp^2 A_\parallel, \tag{83}$$

$$\frac{d}{dt}\left(A_\parallel - d_e^2\nabla_\perp^2 A_\parallel\right) = \eta\nabla_\perp^2 A_\parallel + \rho_s^2\left[n_e + \sqrt{2}g_2, A_\parallel\right] - \frac{1}{\sqrt{2}}\frac{\rho_s}{d_e}\alpha_{Te}\frac{\partial A_\parallel}{\partial y}$$
$$- \frac{\partial\varphi}{\partial z} + \rho_s^2\frac{\partial}{\partial z}\left(n_e + \sqrt{2}g_2\right) \tag{84}$$

$$\frac{dg_2}{dt} = \sqrt{3}\frac{\rho_s}{d_e}\left\{\left[A_\parallel, g_3\right] - \frac{\partial g_3}{\partial z}\right\} + \sqrt{2}\left\{\left[A_\parallel, \nabla_\perp^2 A_\parallel\right] - \frac{\partial}{\partial z}\nabla_\perp^2 A_\parallel\right\}$$
$$- \frac{1}{2}\frac{1}{\rho_s d_e}\alpha_{Te}\frac{\partial\varphi}{\partial y}, \tag{85}$$

$$\frac{dg_m}{dt} = \sqrt{m+1}\frac{\rho_s}{d_e}\left\{\left[A_\parallel, g_{m+1}\right] - \frac{\partial g_{m+1}}{\partial z}\right\} + \sqrt{m}\frac{\rho_s}{d_e}\left\{\left[A_\parallel, g_{m-1}\right] - \frac{\partial g_{m-1}}{\partial z}\right\}$$
$$- m\nu_{ei}g_m + \delta_{m,3}\frac{1}{2}\frac{1}{d_e^2}\alpha_{Te}\frac{\partial A_\parallel}{\partial y}, \quad m > 2, \tag{86}$$

where $\alpha_{Te} = \rho_e/L_{Te}L_\parallel/L_\perp$, with ρ_e the electron Larmor radius and L_{Te} the electron temperature gradient scale length.

References

[1] R. Bruno, V. Carbone, The solar wind as a turbulence laboratory, Liv. Rev. Solar Phys. 2 (2005) 4. doi:10.12942/lrsp-2005-4. URL `http://adsabs.harvard.edu/abs/2005LRSP....2....4B`

[2] B. G. Elmegreen, J. Scalo, Interstellar Turbulence I: Observations and processes, Annu. Rev. Astron. Astrophys. 42 (1) (2004) 211–273. doi:10.1146/annurev.astro.41.011802.094859. URL `http://www.annualreviews.org/doi/abs/10.1146/annurev.astro.41.011802.094859`

[3] K. Shibata, T. Magara, Solar Flares: Magnetohydrodynamic Processes, Liv. Rev. Solar Phys. 8 (2011) 6. doi:10.12942/lrsp-2011-6.

[4] B. Haisch, K. T. Strong, M. Rodono, Flares on the Sun and other stars, Annu. Rev. Astron. Astrophys. 29 (1991) 275–324. doi:10.1146/annurev.aa.29.090191.001423.

[5] D. A. Uzdensky, Magnetic interaction between stars and accretion disks, Astrophys. Space Sci. 292 (1-4) (2004) 573–585. doi:10.1023/B:ASTR.0000045064.93078.87. URL `http://link.springer.com/article/10.1023/B%3AASTR.0000045064.93078.87`

[6] K. Schindler, A theory of the substorm mechanism, J. Geophys. Res. 79 (1974) 2803. doi:10.1029/JA079i019p02803.

[7] J. Wesson, Tokamaks, Oxford University Press, 2011.

[8] E. A. Frieman, L. Chen, Nonlinear gyrokinetic equations for low-frequency electromagnetic waves in general plasma equilibria, Phys. Fluids 25 (1982) 502–508. doi:10.1063/1.863762.
URL http://adsabs.harvard.edu/abs/1982PhFl...25..502F

[9] G. G. Howes, S. C. Cowley, W. Dorland, G. W. Hammett, E. Quataert, A. A. Schekochihin, Astrophysical gyrokinetics: Basic equations and linear theory, Astrophys. J. 651 (2006) 590–614. doi:10.1086/506172.
URL http://adsabs.harvard.edu/abs/2006ApJ...651..590H

[10] X. Garbet, Y. Idomura, L. Villard, T. Watanabe, Gyrokinetic simulations of turbulent transport, Nucl. Fusion 50 (4) (2010) 043002. doi:10.1088/0029-5515/50/4/043002.
URL http://stacks.iop.org/0029-5515/50/i=4/a=043002

[11] J. A. Krommes, The gyrokinetic description of microturbulence in magnetized plasmas, Annu. Rev. Fluid Mech. 44 (1) (2012) 175–201. doi:10.1146/annurev-fluid-120710-101223.
URL http://www.annualreviews.org/doi/abs/10.1146/annurev-fluid-120710-101223

[12] I. G. Abel, G. G. Plunk, E. Wang, M. Barnes, S. C. Cowley, W. Dorland, A. A. Schekochihin, Multiscale gyrokinetics for rotating tokamak plasmas: fluctuations, transport and energy flows, Rep. Progr. Phys. 76 (11) (2013) 116201. doi:10.1088/0034-4885/76/11/116201.
URL http://stacks.iop.org/0034-4885/76/i=11/a=116201

[13] G. G. Howes, W. Dorland, S. C. Cowley, G. W. Hammett, E. Quataert, A. A. Schekochihin, T. Tatsuno, Kinetic simulations of magnetized turbulence in astrophysical plasmas, Phys. Rev. Lett. 100 (6) (2008) 065004. doi:10.1103/PhysRevLett.100.065004.
URL http://link.aps.org/doi/10.1103/PhysRevLett.100.065004

[14] A. A. Schekochihin, S. C. Cowley, W. Dorland, G. W. Hammett, G. G. Howes, E. Quataert, T. Tatsuno, Astrophysical gyrokinetics: Kinetic and fluid turbulent cascades in magnetized weakly collisional plasmas, Astrophys. J. Suppl. 182 (1) (2009) 310. doi:10.1088/0067-0049/182/1/310.
URL http://iopscience.iop.org/0067-0049/182/1/310

[15] G. G. Howes, J. M. TenBarge, W. Dorland, E. Quataert, A. A. Schekochihin, R. Numata, T. Tatsuno, Gyrokinetic simulations of solar wind turbulence from ion to electron scales, Phys. Rev. Lett. 107 (3) (2011) 035004. doi:10.1103/PhysRevLett.107.035004.
URL http://link.aps.org/doi/10.1103/PhysRevLett.107.035004

[16] B. N. Rogers, S. Kobayashi, P. Ricci, W. Dorland, J. Drake, T. Tatsuno, Gyrokinetic simulations of collisionless magnetic reconnection, Phys. Plasmas 14 (9) (2007) 092110. doi:10.1063/1.2774003.
URL http://pop.aip.org/resource/1/phpaen/v14/i9/p092110_s1?isAuthorized=no

[17] M. J. Pueschel, F. Jenko, D. Told, J. Büchner, Gyrokinetic simulations of magnetic reconnection, Phys. Plasmas 18 (11) (2011) 112102. doi:10.1063/1.3656965.
URL http://pop.aip.org/resource/1/phpaen/v18/i11/p112102_s1?isAuthorized=no

[18] R. Numata, W. Dorland, G. G. Howes, N. F. Loureiro, B. N. Rogers, T. Tatsuno, Gyrokinetic simulations of the tearing instability, Phys. Plasmas 18 (11) (2011) 112106. doi:10.1063/1.3659035.
URL http://pop.aip.org/resource/1/phpaen/v18/i11/p112106_s1?isAuthorized=no

[19] J. M. TenBarge, W. Daughton, H. Karimabadi, G. G. Howes, W. Dorland, Collisionless reconnection in the large guide field regime: Gyrokinetic versus particle-in-cell simulations, Phys. Plasmas 21 (2) (2014) 020708. arXiv:1312.5166, doi:10.1063/1.4867068.

[20] P. A. Muñoz, D. Told, P. Kilian, J. Büchner, F. Jenko, Gyrokinetic and kinetic particle-in-cell simulations of guide-field reconnection. Part I: macroscopic effects of the electron flows, ArXiv e-printsarXiv:1504.01351.
URL http://adsabs.harvard.edu/abs/2015arXiv150401351M

[21] A. Zocco, A. A. Schekochihin, Reduced fluid-kinetic equations for low-frequency dynamics, magnetic reconnection, and electron heating in low-beta plasmas, Phys. Plasmas 18 (2011) 2309. doi:10.1063/1.3628639.
URL http://adsabs.harvard.edu/abs/2011PhPl...18j2309Z

[22] M. J. Aschwanden, A. I. Poland, D. M. Rabin, The new solar corona, Annu. Rev. Astron. Astrophys. 39 (1) (2001) 175–210. doi:10.1146/annurev.astro.39.1.175.
URL http://www.annualreviews.org/doi/abs/10.1146/annurev.astro.39.1.175

[23] D. A. Uzdensky, The fast collisionless reconnection condition and the self-organization of solar coronal heating, Astrophys. J. 671 (2) (2007) 2139. doi:10.1086/522915.
URL http://iopscience.iop.org/0004-637X/671/2/2139

[24] W. Gekelman, H. Pfister, Z. Lucky, J. Bamber, D. Leneman, J. Maggs, Design, construction, and properties of the large plasma research device–The LAPD at UCLA, Rev. Sci. Instrum. 62 (12) (1991) 2875–2883. doi:10.1063/1.1142175.
URL http://rsi.aip.org/resource/1/rsinak/v62/i12/p2875_s1?isAuthorized=no

[25] G. Saibene, N. Oyama, J. Lnnroth, Y. Andrew, E. d. l. Luna, C. Giroud, G. T. A. Huysmans, Y. Kamada, M. a. H. Kempenaars, A. Loarte, D. M. Donald, M. M. F. Nave, A. Meiggs, V. Parail, R. Sartori, S. Sharapov, J. Stober, T. Suzuki, M. Takechi, K. Toi, H. Urano, The H–mode pedestal, ELMs and TF ripple effects in JT-60U/JET dimensionless identity experiments, Nucl. Fusion 47 (8) (2007) 969. doi:10.1088/0029-5515/47/8/031.
URL http://iopscience.iop.org/0029-5515/47/8/031

[26] N. F. Loureiro, A. A. Schekochihin, A. Zocco, Fast collisionless reconnection and electron heating in strongly magnetized plasmas, Phys. Rev. Lett. 111 (2013) 025002. doi:10.1103/PhysRevLett.111.025002.
URL `http://link.aps.org/doi/10.1103/PhysRevLett.111.025002`

[27] B. B. Kadomtsev, O. P. Pogutse, Nonlinear helical perturbations of a plasma in the tokamak, Sov. J. Exp. Theo. Phys. 38 (1974) 283–290.
URL `http://adsabs.harvard.edu/abs/1974JETP...38..283K`

[28] H. R. Strauss, Nonlinear, threedimensional magnetohydrodynamics of noncircular tokamaks, Phys. Fluids 19 (1) (1976) 134–140. doi:10.1063/1.861310.
URL `http://pof.aip.org/resource/1/pfldas/v19/i1/p134_s1`

[29] N. F. G. Loureiro, Studies of nonlinear tearing mode reconnection, Ph.D., Imperial College London (University of London) (2005).

[30] N. Loureiro, G. Hammett, An iterative semi-implicit scheme with robust damping, J. Comp. Phys. 227 (9) (2008) 4518–4542. doi:10.1016/j.jcp.2008.01.015.
URL `http://www.sciencedirect.com/science/article/pii/S002199910800034X`

[31] P. B. Snyder, G. W. Hammett, W. Dorland, Landau fluid models of collisionless magnetohydrodynamics, Phys. Plasmas 4 (11) (1997) 3974–3985. doi:10.1063/1.872517.
URL `http://pop.aip.org/resource/1/phpaen/v4/i11/p3974_s1`

[32] T. J. Schep, F. Pegoraro, B. N. Kuvshinov, Generalized twofluid theory of nonlinear magnetic structures, Phys. Plasmas 1 (9) (1994) 2843–2852. doi:10.1063/1.870523.
URL `http://pop.aip.org/resource/1/phpaen/v1/i9/p2843_s1?isAuthorized=no`

[33] S. Gottlieb, C. W. Shu, Total variation diminishing Runge-Kutta schemes, Math. Comp. 67 (1998) 73–85.
URL `http://adsabs.harvard.edu/abs/1998MaCom..67...73G`

[34] S. Pirozzoli, Conservative hybrid compact-WENO schemes for shock-turbulence interaction, J. Comp. Phys. 178 (1) (2002) 81–117. doi:10.1006/jcph.2002.7021.
URL `http://www.sciencedirect.com/science/article/pii/S002199910297021X`

[35] A. Zocco, N. F. Loureiro, D. Dickinson, R. Numata, C. M. Roach, Kinetic microtearing modes and reconnecting modes in strongly magnetised slab plasmas, Plasma Phys. Control. Fusion 57 (6) (2015) 065008.
URL `http://stacks.iop.org/0741-3335/57/i=6/a=065008`

[36] J. A. Krommes, Fundamental statistical descriptions of plasma turbulence in magnetic fields, Phys. Rep. 360 (2002) 1–352. doi:10.1016/S0370-1573(01)00066-7.
URL `http://adsabs.harvard.edu/abs/2002PhR...360....1K`

[37] F. C. Grant, M. R. Feix, Fourier-Hermite solutions of the Vlasov equations in the linearized limit, Phys. Fluids 10 (1967) 696–702. doi:10.1063/1.1762177.
URL `http://adsabs.harvard.edu/abs/1967PhFl...10..696G`

[38] F. C. Grant, M. R. Feix, Transition between Landau and Van Kampen treatments of the Vlasov equation, Phys. Fluids 10 (1967) 1356–1357. doi:10.1063/1.1762288.
URL `http://adsabs.harvard.edu/abs/1967PhFl...10.1356G`

[39] G. Joyce, G. Knorr, H. K. Meier, Numerical integration methods of the Vlasov equation, J. Comp. Phys. 8 (1) (1971) 53–63. doi:10.1016/0021-9991(71)90034-9.
URL `http://www.sciencedirect.com/science/article/pii/0021999171900349`

[40] G. Knorr, M. Shoucri, Plasma simulation as eigenvalue problem, J. Comp. Phys. 14 (1) (1974) 1–7. doi:10.1016/0021-9991(74)90001-1.
URL `http://www.sciencedirect.com/science/article/pii/0021999174900011`

[41] G. W. Hammett, M. A. Beer, W. Dorland, S. C. Cowley, S. A. Smith, Developments in the gyrofluid approach to tokamak turbulence simulations, Plasma Phys. Control. Fusion 35 (8) (1993) 973. doi:10.1088/0741-3335/35/8/006.
URL `http://iopscience.iop.org/0741-3335/35/8/006`

[42] S. A. Smith, Dissipative closures for statistical moments, fluid moments, and subgrid scales in plasma turbulence, Ph.D., Princeton University (1997).
URL `http://w3.pppl.gov/ hammett/sasmith/thesis.html`

[43] H. Sugama, T.-H. Watanabe, W. Horton, Collisionless kinetic-fluid closure and its application to the three-mode ion temperature gradient driven system, Phys. Plasmas 8 (2001) 2617–2628. doi:10.1063/1.1367319.

[44] A. Kanekar, A. A. Schekochihin, W. Dorland, N. F. Loureiro, Fluctuation-dissipation relations for a plasma-kinetic Langevin equation, J. Plasma Phys. 81 (2015) 3004. arXiv:1403.6257, doi:10.1017/S0022377814000622.

[45] A. Zocco, Linear collisionless Landau damping in Hilbert space, Journal of Plasma Physics FirstView (2015) 1–7. doi:10.1017/S0022377815000331.
URL `http://journals.cambridge.org/article_S0022377815000331`

[46] J. T. Parker, P. J. Dellar, Fourier-Hermite spectral representation for the Vlasov-Poisson system in the weakly collisional limit, J. Plasma Phys. 81 (2015) 3003. arXiv:1407.1932, doi:10.1017/S0022377814001287.

[47] L. Gibelli, B. D. Shizgal, Spectral convergence of the Hermite basis function solution of the Vlasov equation: The free-streaming term, J. Comput. Phys. 219 (2) (2006) 477488. doi:10.1016/j.jcp.2006.06.017.
URL `http://dx.doi.org/10.1016/j.jcp.2006.06.017`

[48] G. W. Hammett, F. W. Perkins, Fluid moment models for Landau damping with application to the ion-temperature-gradient instability, Phys. Rev. Lett. 64 (1990) 3019–3022. doi:10.1103/PhysRevLett.64.3019.
URL http://link.aps.org/doi/10.1103/PhysRevLett.64.3019

[49] W. Dorland, G. W. Hammett, Gyrofluid turbulence models with kinetic effects, Phys. Fluids B 5 (1993) 812–835. doi:10.1063/1.860934.

[50] P. B. Snyder, G. W. Hammett, A Landau fluid model for electromagnetic plasma microturbulence, Phys. Plasmas 8 (7) (2001) 3199–3216. doi:10.1063/1.1374238.
URL http://scitation.aip.org/content/aip/journal/pop/8/7/10.1063/1.1374238

[51] V. Borue, S. A. Orszag, Spectra in helical three-dimensional homogeneous isotropic turbulence, Phys. Rev. E 55 (6) (1997) 7005–7009. doi:10.1103/PhysRevE.55.7005.
URL http://link.aps.org/doi/10.1103/PhysRevE.55.7005

[52] T. Y. Hou, R. Li, Computing nearly singular solutions using pseudo-spectral methods, J. Comp. Phys. 226 (1) (2007) 379–397. doi:10.1016/j.jcp.2007.04.014.
URL http://www.sciencedirect.com/science/article/pii/S0021999107001623

[53] S. Godunov, A difference method for numerical calculation of discontinuous solutions of the equations of hydrodynamics, Mat. Sb. (N. S.) 47 (3) (1959) 271–306.
URL http://mi.mathnet.ru/eng/msb4873

[54] G. Strang, On the construction and comparison of difference schemes, SIAM J. Numer. Anal. 5 (1968) 506–517.

[55] J. P. Boyd, Chebyshev and Fourier Spectral Methods, Courier Dover Publications, 2001.

[56] S. A. Orszag, On the elimination of aliasing in finite-difference schemes by filtering high-wavenumber components., J. Atmosph. Sci. 28 (1971) 1074–1074. doi:10.1175/1520-0469(1971)028¡1074:OTEOAI¿2.0.CO;2.
URL http://adsabs.harvard.edu/abs/1971JAtS...28.1074O

[57] T. Grafke, H. Homann, J. Dreher, R. Grauer, Numerical simulations of possible finite time singularities in the incompressible euler equations: Comparison of numerical methods, Phys. D: Nonlin. Phen. 237 (1417) (2008) 1932–1936. doi:10.1016/j.physd.2007.11.006.
URL http://www.sciencedirect.com/science/article/pii/S0167278907004101

[58] T. Y. Hou, Blow-up or no blow-up? A unified computational and analytic approach to 3D incompressible Euler and Navier-Stokes equations, Acta Num. 18 (2009) 277–346. doi:10.1017/S0962492906420018.

[59] P. J. Dellar, Lattice Boltzmann magnetohydrodynamics with current-dependent resistivity, J. Comp. Phys. 237 (2013) 115–131. doi:10.1016/j.jcp.2012.11.021.
URL http://www.sciencedirect.com/science/article/pii/S0021999112007012

[60] R. W. MacCormack, The effect of viscosity in hypervelocity impact cratering, in: Frontiers of Computational Fluid Dynamics, World Scientific, 2002, Ch. 2, pp. 27–43. arXiv:http://www.worldscientific.com/doi/pdf/10.1142/9789812810793_0002, doi:10.1142/9789812810793_0002.
URL http://www.worldscientific.com/doi/abs/10.1142/9789812810793_0002

[61] S. Jardin, Computational Methods in Plasma Physics, CRC Press, 2010.

[62] D. R. Durran, Numerical Methods for Fluid Dynamics: With Applications to Geophysics, Springer, 2010.

[63] E. Anderson, Z. Bai, C. Bischof, S. Blackford, J. Demmel, J. Dongarra, J. Du Croz, A. Greenbaum, S. Hammarling, A. McKenney, D. Sorensen, LAPACK Users'Guide, 3rd Edition, Society for Industrial and Applied Mathematics, Philadelphia, PA, 1999.

[64] R. Samtaney, Numerical aspects of drift kinetic turbulence: Ill-posedness, regularization and a priori estimates of sub-grid-scale terms, Comput. Sci. Disc. 5 (1) (2012) 014004. doi:10.1088/1749-4699/5/1/014004.
URL http://iopscience.iop.org/1749-4699/5/1/014004

[65] H. P. Furth, J. Killeen, M. N. Rosenbluth, Finite-Resistivity instabilities of a sheet pinch, Phys. Fluids 6 (4) (1963) 459–484. doi:10.1063/1.1706761.
URL http://pof.aip.org/resource/1/pfldas/v6/i4/p459_s1?isAuthorized=no

[66] R. Numata, G. G. Howes, T. Tatsuno, M. Barnes, W. Dorland, AstroGK: Astrophysical gyrokinetics code, J. Comp. Phys. 229 (24) (2010) 9347–9372. doi:10.1016/j.jcp.2010.09.006.
URL http://www.sciencedirect.com/science/article/pii/S0021999110005000

[67] F. Militello, F. Porcelli, Simple analysis of the nonlinear saturation of the tearing mode, Phys. Plasmas 11 (5) (2004) L13–L16. doi:10.1063/1.1677089.
URL http://pop.aip.org/resource/1/phpaen/v11/i5/pL13_s1

[68] D. Escande, M. Ottaviani, Simple and rigorous solution for the nonlinear tearing mode, Phys. Lett. A 323 (34) (2004) 278–284. doi:10.1016/j.physleta.2004.02.010.
URL http://www.sciencedirect.com/science/article/pii/S0375960104001781

[69] N. F. Loureiro, S. C. Cowley, W. D. Dorland, M. G. Haines, A. A. Schekochihin, X-point collapse and saturation in the nonlinear tearing mode reconnection, Phys. Rev. Lett. 95 (23) (2005) 235003.

doi:10.1103/PhysRevLett.95.235003.
URL http://link.aps.org/doi/10.1103/PhysRevLett.95.235003

[70] R. Numata, N. F. Loureiro, Ion and electron heating during magnetic reconnection in weakly collisional plasmas, J. Plasma Phys. 81 (2015) 3001. arXiv:1406.6456, doi:10.1017/S002237781400107X.

[71] S. A. Orszag, C.-M. Tang, Small-scale structure of two-dimensional magnetohydrodynamic turbulence, J. Fluid Mech. 90 (01) (1979) 129–143. doi:10.1017/S002211207900210X.

[72] D. Biskamp, H. Welter, Dynamics of decaying twodimensional magnetohydrodynamic turbulence, Phys. Fluids B: Plasma Phys. 1 (10) (1989) 1964–1979. doi:10.1063/1.859060.
URL http://pop.aip.org/resource/1/pfbpei/v1/i10/p1964_s1

[73] H. Politano, A. Pouquet, P. L. Sulem, Current and vorticity dynamics in threedimensional magnetohydrodynamic turbulence, Phys. Plasmas 2 (8) (1995) 2931–2939. doi:10.1063/1.871473.
URL http://scitation.aip.org/content/aip/journal/pop/2/8/10.1063/1.871473

[74] D. Biskamp, E. Schwarz, On two-dimensional magnetohydrodynamic turbulence, Phys. Plasmas 8 (7) (2001) 3282–3292. doi:10.1063/1.1377611.
URL http://pop.aip.org/resource/1/phpaen/v8/i7/p3282_s1?isAuthorized=no

[75] N. F. Loureiro, A. A. Schekochihin, S. C. Cowley, Instability of current sheets and formation of plasmoid chains, Phys. Plasmas 14 (10) (2007) 100703. arXiv:astro-ph/0703631, doi:10.1063/1.2783986.

[76] N. F. Loureiro, A. A. Schekochihin, D. A. Uzdensky, Plasmoid and Kelvin-Helmholtz instabilities in Sweet-Parker current sheets, Phys. Rev. E 87 (1) (2013) 013102. arXiv:1208.0966, doi:10.1103/PhysRevE.87.013102.

[77] N. F. Loureiro, D. A. Uzdensky, A. A. Schekochihin, S. C. Cowley, T. A. Yousef, Turbulent magnetic reconnection in two dimensions, Mon. Not. R. Astron. Soc. 399 (2009) L146–L150. arXiv:0904.0823, doi:10.1111/j.1745-3933.2009.00742.x.

[78] P. S. Iroshnikov, Turbulence of a Conducting Fluid in a Strong Magnetic Field, Astron. Zh. 40 (1963) 742.

[79] R. H. Kraichnan, Inertial-Range Spectrum of Hydromagnetic Turbulence, Phys. Fluids 8 (1965) 1385–1387. doi:10.1063/1.1761412.

[80] R. Kinney, J. C. McWilliams, T. Tajima, Coherent structures and turbulent cascades in twodimensional incompressible magnetohydrodynamic turbulence, Phys. Plasmas 2 (10) (1995) 3623–3639. doi:10.1063/1.871062.
URL http://scitation.aip.org/content/aip/journal/pop/2/10/10.1063/1.871062

[81] P. Goldreich, S. Sridhar, Toward a theory of interstellar turbulence. 2: Strong Alfvénic turbulence, Astrophys. J. 438 (1995) 763–775. doi:10.1086/175121.

[82] S. Bale, P. Kellogg, F. Mozer, T. Horbury, H. Reme, Measurement of the electric fluctuation spectrum of magnetohydrodynamic turbulence, Phys. Rev. Lett. 94 (2005) 215002. doi:10.1103/PhysRevLett.94.215002.
URL http://link.aps.org/doi/10.1103/PhysRevLett.94.215002

[83] O. Alexandrova, J. Saur, C. Lacombe, A. Mangeney, J. Mitchell, S. J. Schwartz, P. Robert, Universality of solar-wind turbulent spectrum from MHD to electron scales, Phys. Rev. Lett. 103 (2009) 165003. doi:10.1103/PhysRevLett.103.165003.
URL http://link.aps.org/doi/10.1103/PhysRevLett.103.165003

[84] S. Boldyrev, J. C. Perez, Spectrum of kinetic-Alfvén turbulence, Astrophys. J. Lett. 758 (2) (2012) L44. doi:10.1088/2041-8205/758/2/L4.
URL http://stacks.iop.org/2041-8205/758/i=2/a=L44

[85] A. Barnes, Collisionless damping of hydromagnetic waves, Phys. Fluids 9 (1966) 1483. doi:10.1063/1.1761882.

[86] J. M. TenBarge, G. G. Howes, W. Dorland, G. W. Hammett, An oscillating Langevin antenna for driving plasma turbulence simulations, Comp. Phys. Comm. 185 (2) (2014) 578–589. doi:10.1016/j.cpc.2013.10.022.
URL http://www.sciencedirect.com/science/article/pii/S0010465513003664

[87] M. Frigo, S. G. Johnson, The design and implementation of FFTW3, Proceedings of the IEEE 93 (2) (2005) 216–231, special issue on "Program Generation, Optimization, and Platform Adaptation".